NASA Technical Paper 3252

1992

Laser Anemometer Measurements and Computations in an Annular Cascade of High Turning Core Turbine Vanes

Louis J. Goldman
and Richard G. Seasholtz
Lewis Research Center
Cleveland, Ohio

National Aeronautics and Space Administration
Office of Management
Scientific and Technical Information Program

Summary

An advanced laser anemometer (LA) was used to measure the mean axial and tangential velocity components in an annular cascade of turbine stator vanes designed for a high bypass ratio engine. These vanes were based on a redesign of the first-stage stator, of a two-stage turbine, that produced 75° of flow turning. Tests were conducted on a 0.771 scale model of the engine size stator. The advanced LA fringe system was designed to employ thinner than usual laser beams resulting in a 50-μm-diameter probe volume (PV). In comparison, this PV was half as large as that in the configurations previously used in this cascade. This smaller size allowed the laser power to be more concentrated in the probe volume permitting measurements to be obtained from smaller seed particles and closer to surfaces. To prevent the beams from uncrossing when passing through the curved optical access window, beam correction optics were employed. In addition, the access window was manufactured to the same high quality as the other optical components used in the LA system.

A particle dynamics calculation for this vane geometry was performed. It indicated that 0.5-μm-diameter seed particles would follow the flow to within ± 0.5 percent (of critical velocity ratio) in both the axial and tangential velocity components. These size particles are representative of the bulk of the aerosol generated by the seeder. Seed particles having 1-μm diameters, which are near the upper end of the seed particle distribution, generally follow the flow to within ± 1 percent (of critical velocity ratio) in both velocity components. However, differences of -2 percent in the tangential velocity component were indicated close to the suction surface of the vanes near the leading-edge region.

Experimental LA measurements of velocity and turbulence were obtained upstream, within, and downstream of the stator vane row at the design exit critical velocity ratio of 0.896 at the hub. Surface static pressure measurements were also obtained near the vane hub, at midspan, and near the tip. The measurements were compared, where possible, with the results from Denton's three-dimensional inviscid flow analysis program. The data are presented in both graphic and tabulated form so that they may be readily used to compare with other turbomachinery computations.

The experimental measurements of vane surface static pressures compared well with the calculated values. The agreement was also, in general, quite good for the velocity component measurements. The laser anemometer measurements indicated that the flow upstream of the vanes was very uniform and axial in direction, in accordance with the design value. Measurements close to the vane suction and pressure surfaces in the leading-edge region indicated the possibility of seed lag problems, as predicted by the particle dynamics calculation. The largest differences between measurement and theory occurred at 80 percent axial chord. The comparison with theory, however, was still felt to be reasonable at this location. The LA measurements downstream of the vanes clearly showed the vane wakes when close to the trailing edge, but the wake deficit quickly dissipated on moving further downstream. Outside the wake regions the measurements were found to agree very well with the inviscid calculations. In general, the turbulence intensity increased as the flow passed through the vane passage and varied from about 2 to 3 percent upstream to 4 to 6 percent downstream of the vanes. Within the vane wakes, turbulence levels as high as 7 to 9 percent were measured.

Introduction

State-of-the-art turbofan engines are characterized by high bypass ratios resulting in high pressure turbines designed for high specific work and low equivalent flows. This can easily produce turbines that have relatively small-sized blading (high hub-to-tip radius ratio), low aspect ratios, and transonic flow stators. All these conditions can be detrimental to engine performance. To alleviate these problems, designers are often forced to specify high turning vanes to increase the blade heights and decrease the flow velocities to more acceptable values. Typical turbines of this type are described in references 1 to 3 as part of the NASA Energy Efficient Engine Program. High turning vanes are also finding use in modern turboshaft applications (ref. 4) as well as in space applications (ref. 5).

However, the use of high turning vanes can result in other problems, such as large secondary flows or, possibly, flow separation. Computer code validation for these adverse conditions is difficult since experimental measurements of the internal flow characteristics of high turning vanes are not commonplace. Some experimental data for high turning vanes have been obtained using pressure probes (refs. 6 and 7) and laser anemometry (ref. 8). But what is generally lacking are the details of the vane geometry and the convenience of tabulated results.

To alleviate this problem, an investigation was performed in an annular cascade of turbine stator vanes designed to produce 75° of flow turning. The stator vanes tested were a second generation design. The original vanes, which were designed to be the first-stage stator of a two-stage high bypass ratio turbine, are described in reference 1. Geometrically the new vanes have a thinner trailing-edge radius and a slightly different pressure surface shape to accommodate the new trailing edge. A 0.771 scale model of the engine size stator was tested herein to minimize changes in the existing facility hardware.

The tests were accomplished in a 508-mm-tip-diameter, ambient-air-inlet cascade described previously in reference 9. The facility was operated at near the design exit-hub-static to inlet-total pressure ratio of 0.605, which corresponds to a critical velocity ratio of 0.896. The untwisted, constant section profile of the vanes, combined with the noncontoured cylindrical endwall geometry, was expected to result in very small radial velocity components. Therefore, measurements of only the axial-tangential velocity components were considered necessary.

An advanced laser anemometer designed for this investigation consisted of a fringe system that employed smaller than usual beam diameters resulting in a 50-μm-diameter probe volume (PV). In comparison, this PV was half as large as that in the configurations previously used in this cascade (refs. 10 and 11). This smaller size allowed the laser power to be more concentrated in the probe volume permitting measurements to be obtained from smaller seed particles and closer to surfaces. The disadvantage of using thinner beam diameters is the tendency of the laser beams to more easily uncross in passing through the curved optical access window. To prevent this from occurring, beam correction optics consisting of an additional zooming cylindrical lens were used. The procedure for designing this lens is described in reference 12. In addition, the access window was manufactured to the same high quality as the other optical components used in the LA system. Similar optical distortion (uncrossing) of the laser beams, for a LA system designed with an 80-μm-diameter probe volume, has been controlled by a special design of the window outer surface contour (ref. 13).

This report presents the results of laser anemometer measurements of velocity and turbulence taken upstream, within, and downstream of the redesigned 75° flow turning vane. The experimental investigation was performed in an annular cascade operating at the design exit critical velocity ratio of 0.896 at the hub. The data obtained represent the results of 35 circumferential surveys taken at constant axial and radial positions in the annular cascade. Surface static pressure measurements were also obtained near the vane hub and tip and at mid-span. The measurements are compared, where possible, with the calculations obtained from Denton's three-dimensional inviscid flow analysis program (ref. 14). This flow analysis previously gave very good comparisons with the laser anemometer measurements obtained for 67° flow turning vanes tested with both cylindrical (ref. 15) and contoured endwalls (ref. 11). The data are presented herein in both graphic and tabulated form so that the measurements can easily be compared to other turbomachinery computations.

Symbols

m number of transverse velocity component measurements (typically 1000)

P total pressure, N/m^2

p static pressure, N/m^2

R radial position, percent of span from hub

s_j^2 variance of the velocity component measurements, $(m/sec)^2$ (eq. (5))

Tu turbulence intensity (eq. (4))

V transverse velocity magnitude, m/sec (fig. 7)

V_{cr} critical velocity (fluid velocity at Mach 1), m/sec

V_j measured velocity component, m/sec (fig. 7)

V_z axial velocity component, m/sec

V_θ tangential velocity component, m/sec

v' velocity fluctuations, m/sec

Z axial position, percent of axial chord from vane leading edge

α flow angle measured from the axial direction, deg (eq. (3); fig. 7)

θ circumferential position, deg

σ standard deviation of velocity component measurements, m/sec

ϕ_j fringe orientation angle, angle between Z-axis and measured velocity component, deg (fig. 7)

Subscripts:

fs free stream

g gas (air)

h hub

LE leading edge of vane

M mixed-out station (fig. 2)

PS pressure surface

p seed particle

SS suction surface

TE trailing edge of vane

0 station at inlet plane of cascade bellmouth (fig. 2)

Superscript:

$-$ mean value

Apparatus

Annular Cascade Facility

The 508-mm-tip-diameter, full-annular, turbine stator cascade includes an inlet section, a test section, and an exit section. A photograph and a cross-sectional view of the facility are shown in figures 1 and 2, respectively. In operation, atmospheric air is drawn through the inlet section, the vanes, and a dump-diffusing exit section before it is exhausted through the laboratory altitude exhaust system.

Prior to entering the altitude exhaust system, the flow passes through a flow-straightening section which removes the swirl created by the stator vanes.

Inlet section.—The inlet, consisting of a bellmouth and a straight section, was designed to accelerate the flow to uniform axial-flow conditions at the vane inlet. The bellmouth profile and coordinates are presented in reference 10.

Test section.—The test section, for this investigation, consists of a full-annular ring of 26 vanes. A cutout in the outer cascade housing provides access for the laser beams to the vane passage as well as to the regions upstream and downstream of the vanes. The vanes in the window region are machined to the vane tip radius so that the window fits flush with the tip endwall. The window is described in the next section.

As indicated in the **Introduction**, the stator vanes were a second generation design. The original vanes were designed (ref. 1) to be the first-stage stator of a two-stage high bypass ratio turbine. Geometrically, the new vanes were designed to have a thinner trailing-edge radius (0.050 cm compared to 0.089 cm) and a slightly different pressure surface shape to accomodate the new trailing edge. The new stator vane geometry and coordinates are shown in figure 3. The untwisted vanes, of constant profile from hub to tip, are stacked at a point on the suction surface, as indicated on figure 3. The vanes have an axial chord of 35.56 mm and a vane height of 38.10 mm, which results in a vane aspect ratio and solidity at the mean radius (based on axial chord) of 1.07 and 0.63, respectively. The vane height is slightly larger than that used in reference 1 (height of 35.64 mm) and was chosen to minimize changes in the existing cascade hardware. The vanes herein tested represent a 0.771 scale model of the engine sized stator (as compared to 0.767 in ref. 1).

Window.—Optical access for the laser beams is provided by a cutout in the cascade housing (fig. 1) that extends upstream and downstream of the vane passage by approximately two and one axial chord, respectively. The window was optically manufactured, under standard lens tolerances, from 3.175-mm-thick optical glass. This was

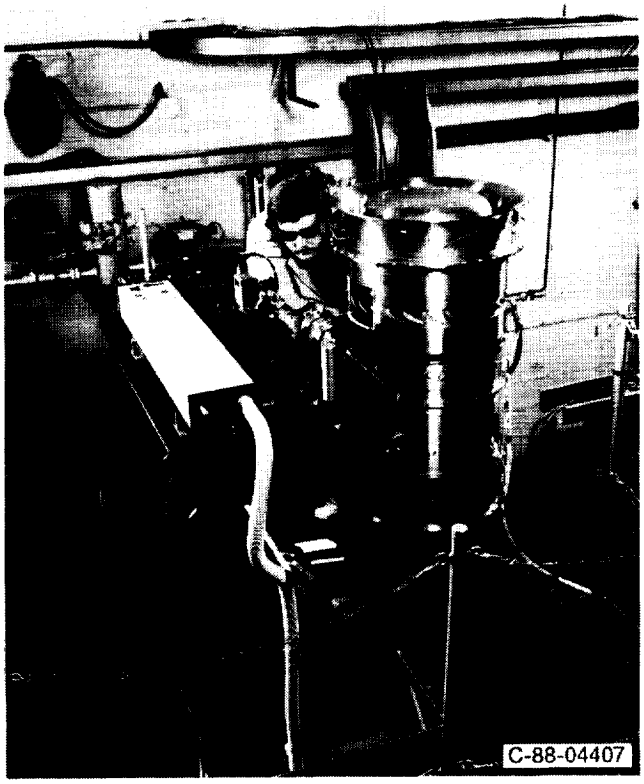

Figure 1.—Core turbine stator annular cascade and laser anemometer.

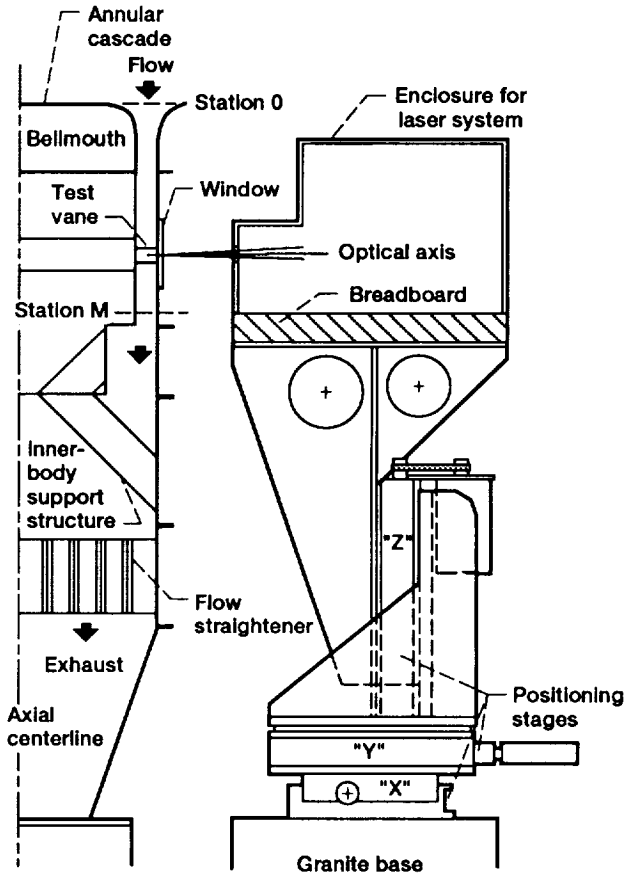

Figure 2.—Schematic cross-sectional view of core turbine stator cascade and laser positioning system.

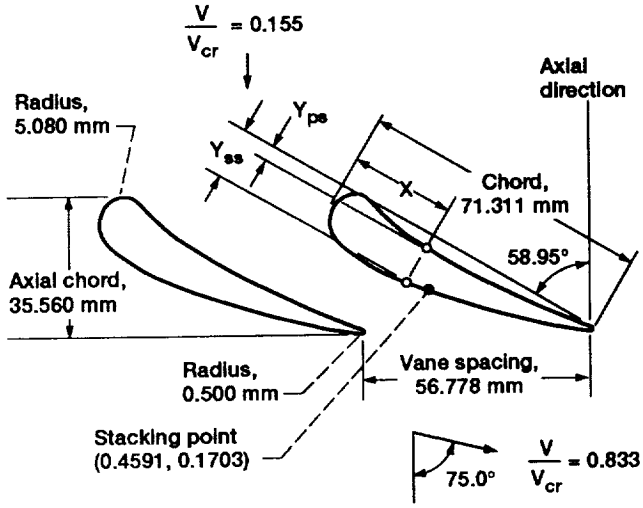

High turning core turbine stator vanes

X	Y_{ps}	Y_{ss}	X	Y_{ps}	Y_{ss}
0	0.0712	0.0712	0.5343	0.0493	0.1532
.0178	.0241	.1231	.5521	.0485	.1488
.0356	.0095	.1460	.5699	.0475	.1443
.0534	.0023	.1616	.5877	.0464	.1397
.0712	0	.1728	.6055	.0453	.1350
.0890	.0023	.1810	.6233	.0440	.1301
.1069	.0085	.1871	.6411	.0426	.1252
.1247	.0145	.1918	.6589	.0411	.1202
.1425	.0198	.1953	.6768	.0396	.1151
.1603	.0245	.1979	.6946	.0379	.1099
.1781	.0286	.1996	.7124	.0362	.1047
.1959	.0323	.2007	.7302	.0344	.0993
.2137	.0356	.2011	.7480	.0325	.0939
.2315	.0384	.2010	.7658	.0305	.0884
.2493	.0410	.2004	.7836	.0285	.0829
.2671	.0431	.1994	.8014	.0264	.0773
.2850	.0450	.1980	.8192	.0242	.0717
.3028	.0466	.1962	.8370	.0220	.0660
.3206	.0480	.1942	.8549	.0197	.0603
.3384	.0491	.1919	.8727	.0173	.0545
.3562	.0500	.1893	.8905	.0149	.0487
.3740	.0507	.1865	.9083	.0124	.0428
.3918	.0512	.1835	.9261	.0099	.0369
.4096	.0515	.1802	.9439	.0073	.0310
.4274	.0516	.1768	.9617	.0047	.0250
.4452	.0516	.1732	.9795	.0020	.0189
.4630	.0514	.1695	.9973	.0015	.0125
.4809	.0511	.1656	1.0000	.0070	.0070
.4987	.0507	.1616			
.5165	.0500	.1574			

(All values nondimensionalized by chord, 71.311 mm (2.8075 in.))

Figure 3.—High turning core turbine stator vane geometry at mean section.

necessary because of the smaller laser beam diameters employed in the optical design and the possibility of the beams uncrossing when passing through the window. A silicone rubber sealing material is used to seal both the window to the cascade housing and to seal the vane tips to the window. The window covered about 36° in the circumferential direction and was 140 mm high.

Laser Anemometer System

For this investigation, an advanced laser anemometer was designed and consisted of a fringe system that employed smaller than usual beam diameters resulting in a 50-μm-diameter probe volume. A description of the optics, positioning system, and calibration procedures used in the investigation is presented in this section.

Optical layout.—A photograph of the laser anemometer and a schematic of the optical layout are shown in figures 1 and 4, respectively. The argon-ion laser has a maximum output power of 1.5 W at a 514.5-nm wavelength with a vertically polarized TEM_{00} transverse mode. Lenses L1 and L2 (focal lengths of 80 mm and 100 mm, respectively) function as mode-matching lenses to position the beam waists at the focal plane of lens L5. The beam divider (constructed from two appropriately

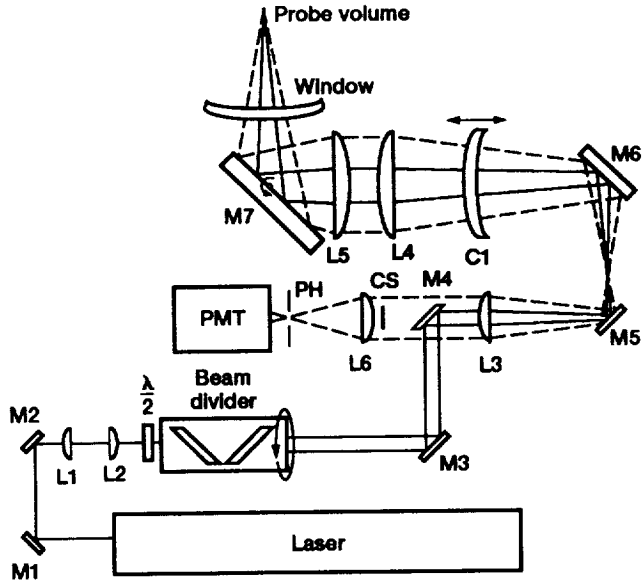

Figure 4.—Optical configuration of laser anemometer measurement system.

coated 6.35-mm-thick fused silica plates) splits the single beam into two equal intensity parallel beams (~ 10-mm separation). The divider is mounted in a motor-driven rotary mount so that the orientation of the fringes can be set at any desired angle. A half-wave retardation plate (gear driven by the mount at one-half the angle of rotation of the divider) is located at the input of the beam divider to maintain the proper linear polarization at the input of the beam divider. After reflection from mirrors M3 and M4, the parallel beams from the beam splitter are expanded by lenses L3 (200-mm focal length) and L4 (500-mm focal length) to approximately 25-mm spacing. Mirror M4 is elliptical with a minor axis of 15.2 mm and major axis of 21.6 mm. This was done to minimize the blockage by the mirror (M4) of the scattered light collected by the receiving optics. The beams are then focused by lens L5 (250-mm focal length) to cross at the probe volume after being reflected by mirror M7. Mirror M7 is mounted on a motor-driven goniometer stage with its axis perpendicular to the plane of the optical table. This enables the optical axis to be positioned along the radial direction in the stator cascade. The diameter ($1/e^2$ intensity) of the probe volume is about 50 μm and the fringe spacing is 5.2 μm (about 10 fringes). The technique used to measure the fringe spacing is described in appendix B of reference 11. Light scattered from seed particles passing through the probe volume (after reflection by M7) is collimated by lens L5 and reduced to a 40-mm-diameter parallel beam by lenses L4 and L3. A central circular stop CS (diameter of 32 mm) placed between mirror M4 and lens L6 is used to reduce the effective length of the probe volume. This mask blocked 64 percent of the full clear aperture of the collection lens L5, which means the receiving optics had an effective f-number for light collection of f/4.2. The scattered light beam is focused by lens L6 (200-mm focal length) through a 100-μm-diameter pinhole (PH) located in front of photomultiplier PMT (RCA 4526). The system magnification of 2 results in the image of the PH at the probe volume having a 50-μm diameter. The signal from the PMT is processed by a counter-type processor to provide velocity components transverse to the optical axis.

Cylindrical lens C1 is used to correct the astigmatism introduced by the window (ref. 12). This ensures that the two beams cross at the probe volume for all orientations of the fringe pattern. The cylindrical lens C1 (BK7, with radii of curvature of 129.6 mm and 134.1 mm and center thickness of 5 mm) was custom designed for this application. It is mounted on a remotely controlled linear translation stage with the cylinder axis perpendicular to the optical table. (The axial position of the lens needed to minimize the astigmatism is a function of the distance of the probe volume from the window.)

Positioning system.—The laser and optics are mounted on a 610-mm- by 1524-mm- by 64-mm-thick aluminum optical breadboard. The breadboard is mounted on a three-axis linear positioning system with an accuracy of ± 2.5 μm per 25 mm (not to exceed ± 12 μm per 300 mm of travel). The positioning system ANORAD Corporation controller is located in the test cell near the cascade and is connected with an RS–232 serial communications link to the minicomputer located in the control room. In addition to the three linear stages, the beam divider and goniometer mounted mirror are also controlled with this system. The positioning system provides a sufficient number of degrees of freedom to allow the optical axis to be directed along a radial line throughout the test region. The window correction optics cylindrical lens was positioned with a separate Newport Corporation linear actuator and translation stage.

Calibration procedures.—A critical requirement for obtaining laser anemometer data for computer code verification is the accurate determination of the probe volume location relative to the experimental hardware. For the stator cascade described herein, location accuracies of 25 μm are desired. A complicating factor in achieving this accuracy is the movement of the stator cascade relative to the laser anemometer when going from static to flow conditions and when the ambient temperature changes. Because of these reasons, position calibration must be checked under test conditions. The parameters required are the coordinates of the cascade axes, the radial position of the hub endwall, and the circumferential location of the suction and pressure surfaces of the vanes at a given axial and radial position. The details of most of the calibration procedures used in this investigation are presented in appendix B of reference 11 and are not discussed further herein. One additional calibration technique required to determine the position of the window correction optics relative to the cascade is now described.

The position calibration for the window correction optics was accomplished by first focusing the probe volume on a metal surface (at a known radial position) in the cascade (the hub endwall or a metal block resting on the vane leading edges). The scattered light collected through the receiving PH was passed through a microscope objective and the magnified image projected onto a screen for easier observation. The position of the correction optics lens was then adjusted so that the spot size of the collected light was minimized. The fringe pattern was also rotated through 360° to ensure that the spot size and shape did not change; a change would have indicated that the laser beams had uncrossed and the correction optics were not at the correct position. It was found that, for this optical configuration, a linear relationship between the distance of the correction optics lens to the focusing lens and the distance of the probe volume from the window provided a good fit of the calibration data.

Seeding.—An organic aerosol (Rosco fog/smoke fluid) was used as the seed material for these tests. The fluid was atomized with a commercial TSI, Inc., six-jet aerosol generator. The seed was then passed through a separator to remove any large droplets before being injected through a 6-mm-diameter tube into the flow at the entrance of the bellmouth. Measuring the seed particle size distribution over a 0.09- to 3.00-μm-diameter range was performed at the bellmouth entrance using a Particle Measuring Systems, Inc., laser aerosol spectrometer. The results, shown in figure 5, indicate that most of the seed

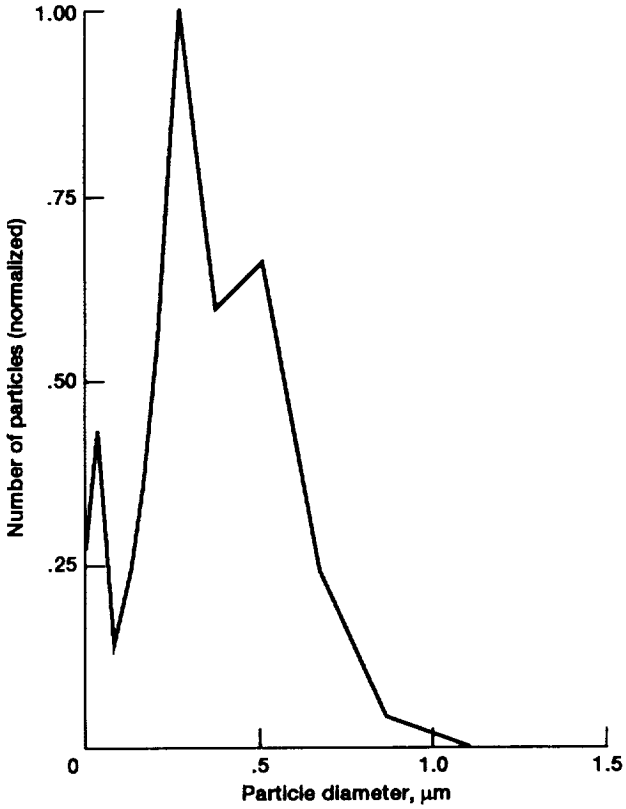

Figure 5.—Measured seed particle size distribution.

particles produced are between 0.3 and 0.6 μm diameter with very few greater than 1.0 μm.

Test Procedure

Cascade Flow Conditions

The test conditions in the cascade were set by controlling the pressure ratio across the vane row with two throttle valves located in the exhaust system. A hub static tap located downstream of the test section, where the flow was assumed to be nearly circumferentially uniform (station M, fig. 2), was used to set this pressure ratio. For this investigation, the exit hub static to inlet total pressure ratio $p_{h,M}/P_0$ was maintained at the design value of 0.605. This corresponds to a critical velocity ratio of 0.896.

Survey Measurement Locations

The location of the laser anemometer survey measurements are summarized in figure 6. Circumferential surveys were made at 11 axial stations (every 10 percent of axial chord) within the vane passage, 4 axial stations upstream, and 6 axial stations downstream of the vanes. The nomenclature and orientation of the velocity component measurements are shown in figure 7. At a given axial station, laser surveys were made

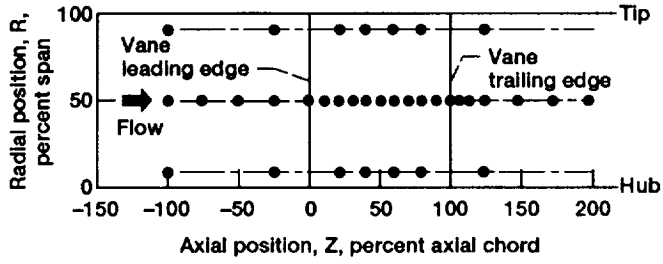

Figure 6.—Laser survey measurement locations.

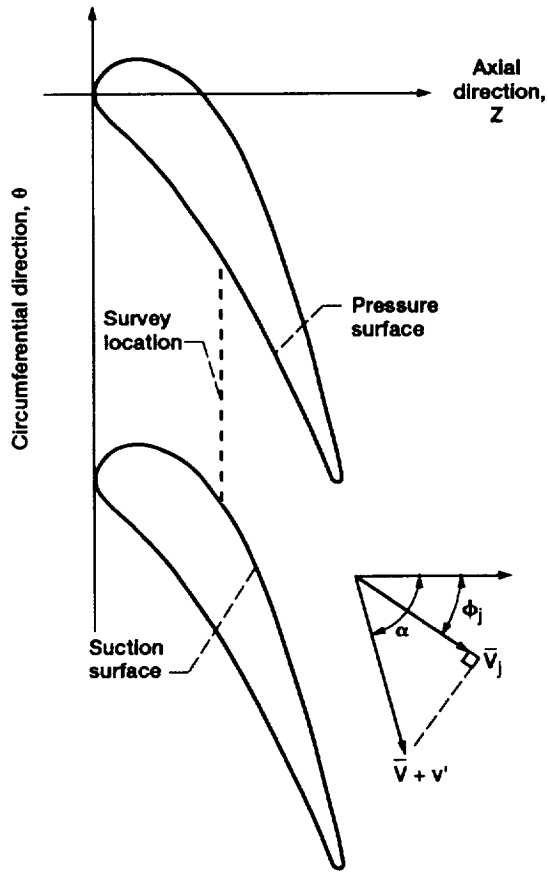

Figure 7.—Nomenclature of velocity component measurements for laser anemometer surveys.

across the vane passage, at one or more fixed radial positions, with circumferential increments between 0.5° to 0.8°. At the vane mean radius, survey measurements were obtained at all 21 axial stations. Near the hub and the tip (i.e., radial positions of 10 and 90 percent of span) measurements were made at 7 axial stations (fig. 6). The 35 circumferential surveys taken resulted in over 700 distinct measurement points. At every fixed point in the flow field seven components of the transverse velocity V_j were measured at 10° intervals centered about the expected flow direction (see fig. 7). These measurements were made by rotating the beam divider, thereby changing the fringe pattern orientation with respect to the flow direction. This allowed not only the axial and tangential velocity components

to be determined by a least-squares procedure but it also provided an estimate of their statistical accuracy.

Data Acquisition

A Digital Equipment Corporation PDP-11/44 minicomputer was used to control the optical positioning system and to acquire the laser anemometer data. The fringe signal from the PMT was processed with a counter-type processor using four cycles of the Doppler burst. The counter output data, consisting of Doppler frequency and time-between-measurements, were transferred to the minicomputer via a DMA interface having a maximum transfer rate of about 200 kHz. As stated previously, data were taken at seven fringe orientations for each measurement position; this being restricted by the 64K byte program size limit of the minicomputer. At each fringe orientation, 1000 data pairs were taken. The frequency data (corresponding to velocity components) were stored in 256 bin histograms for later off-line processing. Typical data rates ranged from 5 to 50 kHz.

Calculation Procedures

Experimental

The measured fringe spacing (5.2 μm) is used to calculate the mean velocity component $\overline{V}_j$ and the variance s_j^2 from the stored 256 bin frequency histogram. This is done for the seven fringe orientation angles ϕ_j at each measurement location. The mean axial velocity component $\overline{V}_z$ and tangential velocity component $\overline{V}_\theta$ (of the projection of the velocity vector in the axial-tangential plane, fig. 7) are then obtained using a procedure similar to that described in references 11 and 15. That is, $\overline{V}_z$ and $\overline{V}_\theta$ are found using a least-squares fit to

$$\overline{V}_j = \overline{V}_z \cos \phi_j + \overline{V}_\theta \sin \phi_j \tag{1}$$

In addition, the least-squares fit provides an estimate of the statistical uncertainty in the calculated velocity components. The mean transverse velocity magnitude $\overline{V}$ and mean flow angle $\overline{\alpha}$ can be calculated from

$$\overline{V} = \sqrt{\overline{V}_z^2 + \overline{V}_\theta^2} \tag{2}$$

and

$$\overline{\alpha} = \arctan\left(\frac{\overline{V}_\theta}{\overline{V}_z}\right) \tag{3}$$

For isotropic turbulence, and in the absence of noise from the laser, the turbulence intensity Tu of the flow is calculated from

$$Tu = \frac{\sqrt{v'^2}}{\overline{V}} \tag{4}$$

The mean velocity fluctuations v'^2 for isotropic turbulence are obtained by a least-squares fit of (see ref. 15)

$$s_j^2 = \frac{1}{m}\sum_{j=1}^{m} (V_j - \overline{V}_j)^2 = v'^2[1 - \sin 2(\overline{\alpha} - \phi_j)] \tag{5}$$

It is assumed that $\overline{\alpha}$ has been determined previously using equation (3).

Theoretical

Theoretical calculations were performed to determine the velocity of the air flowing through the vane passage and to determine how well the entrained seed particles used for the laser anemometer measurements tracked the airflow.

Air velocity.—The velocity field for the 75° turning vane was calculated using Denton's three-dimensional inviscid flow analysis program (ref. 14). Denton's program is a time-marching, finite-volume solution of the Euler equations. The static pressure is specified at the downstream hub location, and the spanwise pressure variation is calculated by the program assuming zero meridional streamline curvature (simple radial equilibrium). Cusps are placed at the leading and trailing edges of the vanes to minimize discontinuities in the grid slope. The cusps carry no load and, therefore, flow periodicity is automatically satisfied by the program. Denton's calculations were selected for comparison with the experimental data reported herein because they were found to compare well with the laser measurements obtained previously (refs. 11 and 15) in this cascade.

Seed particle velocity.—A dynamics calculation was performed for this vane geometry to determine how well different sized seed particles tracked the airflow. The seed particle trajectories were calculated for a mean-radius, blade-to-blade stream surface by the method described in reference 16. It is assumed for these calculations that the particles are moving through a known airflow (velocity field). Furthermore, the seed particles are only acted on by viscous drag forces and that these forces follow Stoke's law. The particle concentration is also low enough so as not to influence the airflow or the air properties. In addition, the seed particles are spherical, of uniform size, non-interacting, and uniformally distributed in the airflow. The difference between the calculated particle velocity and the airflow velocity, at a given point, is an estimate of how well the particles (of assumed size) follow the flow.

Results and Discussion

Seed Particle Velocity

The results of the seed particle dynamics calculation are shown in figure 8 for 0.5- and 1-μm-diameter particles. Results

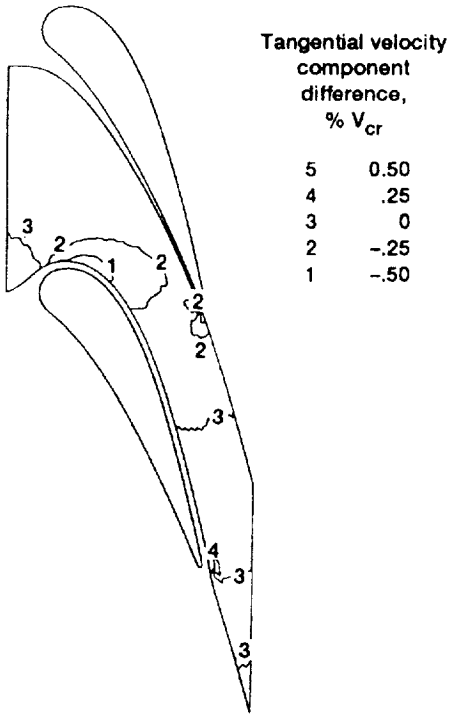

(a) Tangential velocity component difference, $(|V_{p,\theta}| - |V_{g,\theta}|)/V_{cr}$, percent (0.5–μm diameter particles).

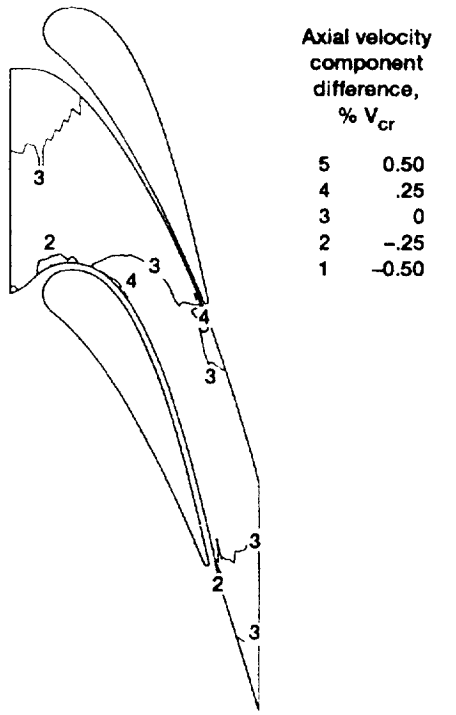

(b) Axial velocity component difference, $(|V_{p,z}| - |V_{g,z}|)/V_{cr}$, percent (0.5–μm diameter particles).

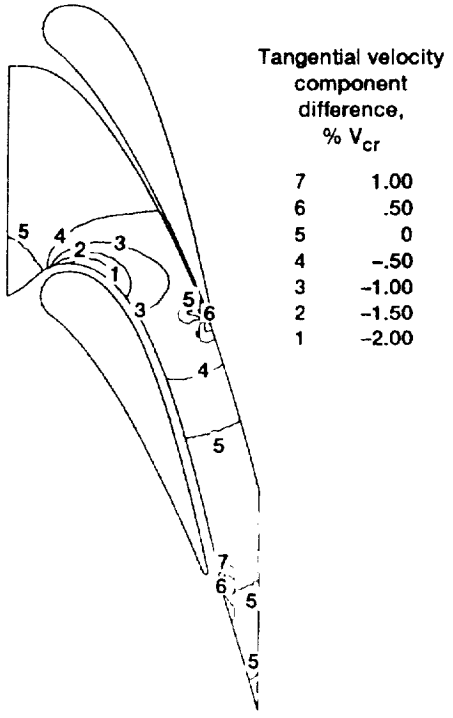

(c) Tangential velocity component difference, $(|V_{p,\theta}| - |V_{g,\theta}|)/V_{cr}$, percent (1.0–μm diameter particles).

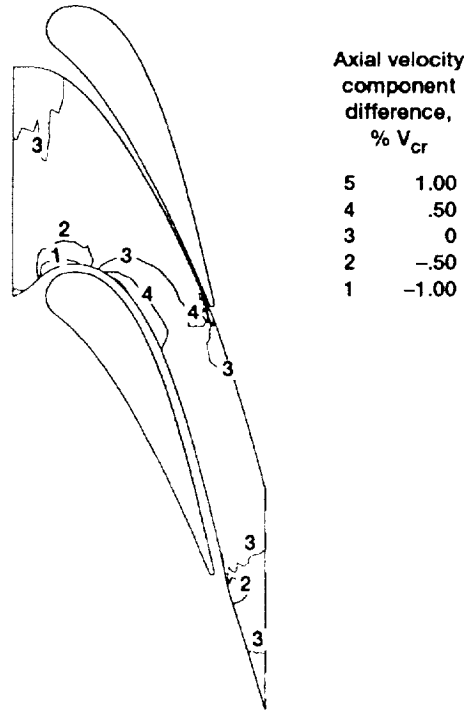

(d) Axial velocity component difference, $(|V_{p,z}| - |V_{g,z}|)/V_{cr}$, percent (1.0–μm diameter particles).

Figure 8.—Dynamic behavior of seed particles entrained in airflow through vanes at mean radius.

are presented for both the axial and tangential components of velocity since this is the form used for the experimental LA measurement presentations. Contour lines in this figure are shown as differences in the seed particle and the airflow component velocities normalized by the critical velocity. Negative contour levels, therefore, represent seed particles lagging the airflow.

The 0.5-μm-diameter particles are representative of the size of the bulk of the aerosol generated (see fig. 5). These results (figs. 8(a) and (b)) indicated that differences in the seed particle and the airflow velocities are less than ± 0.5 percent (in critical velocity ratio) in both components, with most of the flow less than ± 0.25 percent. The 1-μm-diameter particles are near the upper end of the seed particle distribution produced by the aerosol generator (fig. 5). As such, these dynamic calculations represent an estimate of the maximum lag problems that can occur in the LA measurements. In general, the contour levels for both velocity components are less than ± 1 percent (figs. 8(c) and (d)). However, tangential velocity component contours of -2 percent exist close to the suction surface of the vane near the leading-edge region.

Surface Static Pressure Measurements

Static pressures were measured on the vane surface for radial positions of 6.7, 50, and 93.3 percent of span and are presented in figure 9 as free-stream critical velocity ratios. The experimental pressure ratio measurements are also given in table I. Comparison of the vane surface measurements and the theoretical results from Denton's inviscid flow analysis program generally show good agreement. However, at 50 and 93.3 percent span, the measurements indicate slightly more vane loading over most of the surface than do the calculations.

Laser Survey Measurements

The laser survey measurements are presented in figures 10 to 30 for 11 axial planes within the vane passage and for 10 axial planes upstream and downstream of the vanes. Measurements at the vane mean radius were made at all 21 axial stations. As indicated in figure 6, measurements at 10 and 90 percent of span were obtained at 7 axial stations. Previous investigations in this cascade (refs. 10 and 11), required the use of a fluorescent dye technique (ref. 17) to obtain LA measurements at 10 and 90 percent of span. This dye technique was not required with the advanced LA system designed with a 50-μm-diameter probe volume and used herein.

The experimental data are presented as axial and tangential critical velocity ratios as functions of circumferential positions. These values are also given in table II. In addition, the circumferential locations of the vane suction and pressure surfaces, which are used in the data presentation figures, are given in table III. The estimated statistical uncertainties of the measurements (as determined by the methods described in ref.

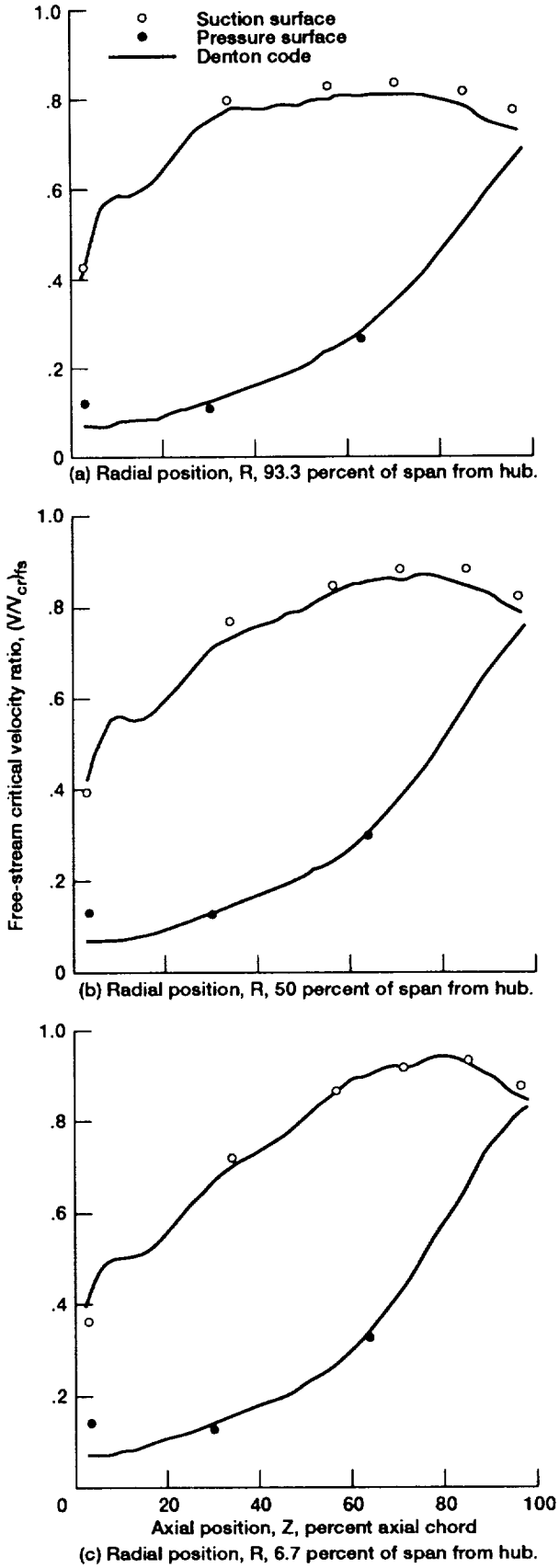

Figure 9.—Comparison of vane free-stream critical velocity ratio and theory.

TABLE I.—VANE SURFACE STATIC PRESSURE MEASUREMENTS FOR HIGH TURNING TURBINE STATOR AT DESIGN PRESSURE RATIO

Radial position, R, percent	Axial position, Z, percent	Suction surface pressure ratio, p_{ss}/P_0	Pressure surface pressure ratio, p_{ps}/P_0
6.7	2.65	0.924	----
	34.44	.730	----
	56.58	.627	----
	71.11	.592	----
	85.43	.578	----
	96.29	.618	----
	3.30	----	0.989
	30.29	----	.991
	63.76	----	.939
50.0	2.65	0.911	----
	34.44	.695	----
	56.58	.642	----
	71.11	.617	----
	85.43	.614	----
	96.29	.655	----
	3.30	----	0.991
	30.29	----	.992
	63.76	----	.949
93.3	2.65	0.898	----
	34.44	.673	----
	56.58	.656	----
	71.11	.649	----
	85.43	.660	----
	96.29	.691	----
	3.30	----	0.991
	30.29	----	.993
	63.76	----	.959

TABLE II.—LASER ANEMOMETER MEASUREMENTS FOR HIGH TURNING TURBINE STATOR VANE AT DESIGN PRESSURE RATIO

Axial position, Z, percent	Radial position, R, percent	Tangential position, θ, deg	Axial velocity ratio, V_z/V_{cr}	Standard deviation, σ/V_{cr}	Circumferential velocity ratio, V_θ/V_{cr}	Standard deviation, σ/V_{cr}	Turbulence intensty, Tu, percent
−100.0	10.0	262.00	0.164	0.001	0.003	0.003	2.2
		263.00	.164	.001	.002	.003	2.1
		264.00	.165	.001	.003	.003	2.3
		265.00	.165	.001	.003	.003	2.8
		266.00	.166	.001	.006	.003	2.4
		267.00	.166	.001	.005	.002	2.1
		268.00	.166	.001	.007	.002	2.2
		269.00	.165	.001	.006	.003	2.0
		270.00	.165	.001	.005	.002	1.9
		271.00	.163	.001	.005	.003	2.1
		272.00	.163	.001	.005	.003	2.1
		273.00	.163	.001	.003	.003	2.0
		274.00	.163	.001	.003	.002	1.9
		275.00	.163	.001	.002	.003	2.1
		276.00	.163	.001	.002	.003	2.0
		277.00	.164	.001	.001	.003	2.2
−100.0	50.0	262.00	0.164	0.001	−0.000	0.002	2.0
		263.00	.165	.001	−.001	.002	2.2
		264.00	.166	.001	−.000	.003	2.1
		265.00	.166	.000	.000	.001	2.1
		266.00	.167	.001	.000	.002	2.0
		267.00	.166	.001	.002	.002	2.2
		268.00	.166	.001	.002	.002	2.1
		269.00	.165	.001	.003	.002	2.0
		270.00	.164	.001	.003	.002	1.9
		271.00	.164	.001	.002	.003	1.9
		272.00	.163	.001	.002	.002	1.9
		273.00	.163	.001	.001	.003	1.8
		274.00	.164	.001	.003	.002	2.0
		275.00	.164	.001	.000	.003	2.0
		276.00	.164	.001	.001	.002	2.0
		277.00	.165	.001	−.001	.002	2.1
−100.0	90.0	262.00	0.163	0.001	0.006	0.003	2.4
		263.00	.164	.001	.003	.002	2.7
		264.00	.164	.001	.002	.004	2.8
		265.00	.165	.001	.004	.004	3.2
		266.00	.164	.002	.004	.005	3.4
		267.00	.165	.002	.004	.004	3.0
		268.00	.165	.001	.008	.003	3.9
		269.00	.165	.001	.004	.002	2.5
		270.00	.162	.002	.008	.005	3.6
		271.00	.161	.001	.004	.004	3.4
		272.00	.162	.001	.006	.002	2.7
		273.00	.162	.002	.003	.005	3.0
		274.00	.162	.001	.003	.003	3.1
		275.00	.162	.002	.003	.005	2.8
		276.00	.163	.002	.001	.004	3.3
		277.00	.163	.001	.007	.003	3.8
−75.0	50.0	262.00	0.163	0.001	−0.003	0.003	1.8
		263.00	.166	.001	−.004	.002	2.0
		264.00	.168	.001	−.002	.002	2.1
		265.00	.170	.000	−.002	.001	2.2
		266.00	.170	.001	−.002	.002	2.0
		267.00	.170	.001	.003	.001	2.3

TABLE II.—Continued.

Axial position, Z, percent	Radial position, R, percent	Tangential position, θ, deg	Axial velocity ratio, V_z/V_{cr}	Standard deviation, σ/V_{cr}	Circumferential velocity ratio, V_θ/V_{cr}	Standard deviation, σ/V_{cr}	Turbulence intensty, Tu, percent
−75.0	50.0	268.00	0.169	0.000	0.004	0.001	2.3
		269.00	.167	.000	.003	.001	2.1
		270.00	.165	.001	.003	.002	1.9
		271.00	.163	.001	.003	.002	1.9
		272.00	.162	.001	.002	.002	1.8
		273.00	.161	.001	.002	.003	1.8
		274.00	.161	.001	−.000	.002	1.8
		275.00	.162	.001	−.001	.003	1.8
		276.00	.164	.001	−.002	.003	1.9
		277.00	.166	.001	−.003	.002	2.3
−50.0	50.0	262.00	0.160	0.001	−0.008	0.003	1.8
		263.00	.166	.001	−.010	.002	2.1
		264.00	.173	.001	−.009	.003	2.5
		265.00	.178	.001	−.005	.004	2.4
		266.00	.180	.001	−.001	.004	2.4
		267.00	.179	.001	.004	.004	2.3
		268.00	.175	.001	.007	.003	2.4
		269.00	.170	.001	.010	.002	2.5
		270.00	.164	.001	.010	.002	2.0
		271.00	.160	.001	.007	.002	1.7
		272.00	.157	.001	.006	.003	1.7
		273.00	.155	.001	.003	.003	1.7
		274.00	.155	.001	−.002	.003	1.7
		275.00	.157	.001	−.005	.003	1.7
		276.00	.161	.001	−.007	.002	1.9
		277.00	.167	.001	−.011	.002	2.3
−25.0	10.0	262.00	0.142	0.001	−0.025	0.002	3.6
		263.00	.155	.001	−.032	.004	2.5
		264.00	.177	.001	−.030	.004	4.0
		265.00	.192	.001	−.021	.004	3.1
		266.00	.197	.001	−.004	.004	2.4
		267.00	.193	.002	.010	.006	2.1
		268.00	.186	.002	.020	.005	2.3
		269.00	.175	.001	.022	.004	3.0
		270.00	.163	.001	.021	.002	2.5
		271.00	.154	.001	.022	.003	2.6
		272.00	.147	.001	.022	.003	2.7
		273.00	.141	.001	.016	.003	2.7
		274.00	.134	.001	−.000	.004	3.9
		275.00	.135	.002	−.020	.005	4.6
		276.00	.144	.001	−.031	.002	2.1
		277.00	.157	.001	−.035	.004	2.8
−25.0	50.0	262.00	0.145	0.001	−0.035	0.002	2.0
		263.00	.165	.001	−.040	.003	2.6
		264.00	.191	.001	−.038	.003	2.3
		265.00	.202	.001	−.021	.002	1.8
		266.00	.204	.001	−.001	.002	1.8
		267.00	.200	.001	.019	.004	1.7
		268.00	.189	.001	.025	.002	2.1
		269.00	.177	.001	.027	.003	2.3
		270.00	.164	.001	.025	.002	2.4
		271.00	.154	.001	.026	.003	1.9
		272.00	.146	.001	.022	.003	2.0
		273.00	.139	.001	.015	.003	2.6

TABLE II.—Continued.

Axial position, Z, percent	Radial position, R, percent	Tangential position, θ, deg	Axial velocity ratio, V_z/V_{cr}	Standard deviation, σ/V_{cr}	Circumferential velocity ratio, V_θ/V_{cr}	Standard deviation, σ/V_{cr}	Turbulence intensty, Tu, percent
−25.0	50.0	274.00	0.133	0.001	−0.005	0.004	3.2
		275.00	.136	.001	−.024	.003	2.8
		276.00	.147	.001	−.037	.002	1.6
		277.00	.170	.002	−.038	.005	2.7
−25.0	90.0	262.00	0.153	0.001	−0.030	0.004	2.6
		263.00	.175	.001	−.049	.002	5.3
		264.00	.201	.002	−.028	.004	2.1
		265.00	.209	.001	−.006	.004	2.3
		266.00	.207	.001	.016	.003	2.2
		267.00	.199	.001	−.029	.003	2.2
		268.00	.186	.002	.035	.005	3.5
		269.00	.175	.001	.036	.004	3.2
		270.00	.159	.002	.036	.004	3.6
		271.00	.149	.001	.032	.003	4.4
		272.00	.142	.001	.031	.003	3.8
		273.00	.135	.002	.010	.006	3.8
		274.00	.131	.002	−.001	.004	5.9
		275.00	.137	.002	−.027	.004	6.0
		276.00	.154	.001	−.034	.003	3.9
		277.00	.182	.002	−.041	.005	3.9
0.0	50.0	263.25	0.222	0.001	−0.192	0.002	3.5
		263.50	.261	.002	−.154	.003	2.9
		263.75	.280	.001	−.127	.002	2.6
		264.00	.291	.001	−.101	.002	2.4
		264.50	.296	.001	−.047	.002	2.6
		265.00	.289	.000	−.017	.001	2.3
		265.50	.277	.001	.007	.001	2.3
		266.00	.263	.001	.032	.002	2.4
		266.50	.249	.000	.038	.001	2.1
		267.00	.236	.001	.050	.002	2.2
		267.50	.222	.001	.053	.001	2.3
		268.00	.209	.001	.058	.002	2.4
		268.50	.197	.001	.063	.003	2.3
		269.00	.186	.001	.067	.002	2.2
		269.50	.175	.001	.070	.003	2.2
		270.00	.164	.001	.062	.001	2.3
		270.50	.154	.001	.062	.001	2.6
		271.00	.144	.000	.060	.001	2.7
		271.50	.136	.000	.054	.001	3.1
		272.00	.126	.000	.051	.001	3.0
		272.50	.118	.001	.046	.002	3.0
		273.00	.109	.000	.040	.001	3.1
		273.50	.099	.001	.034	.001	3.3
		274.00	.086	.001	.026	.001	4.3
		274.50	.073	.001	.018	.001	5.2
10.0	50.0	263.60	0.463	0.001	−0.170	0.002	2.4
		263.80	.440	.001	−.118	.001	2.3
		264.00	.420	.001	−.077	.001	2.3
		264.20	.402	.001	−.048	.002	2.0
		264.50	.377	.001	−.018	.002	2.6
		265.00	.344	.001	.016	.002	2.3
		265.50	.314	.001	.044	.002	2.2
		266.00	.290	.000	.058	.001	2.0
		266.50	.268	.001	.074	.003	2.0

TABLE II.—Continued.

Axial position, Z, percent	Radial position, R, percent	Tangential position, θ, deg	Axial velocity ratio, V_z/V_{cr}	Standard deviation, σ/V_{cr}	Circumferential velocity ratio, V_θ/V_{cr}	Standard deviation, σ/V_{cr}	Turbulence intensty, Tu, percent
10.0	50.0	267.00	0.248	0.001	0.079	0.002	2.4
		267.50	.230	.001	.086	.001	2.5
		268.00	.213	.001	.088	.001	2.5
		268.50	.198	.001	.089	.002	2.3
		269.00	.184	.001	.091	.002	2.2
		269.50	.170	.001	.092	.002	2.4
		270.00	.158	.002	.087	.003	2.6
		270.50	.145	.002	.083	.002	3.4
		271.00	.133	.002	.080	.003	2.5
		271.50	.128	.002	.073	.002	2.3
		272.00	.117	.002	.069	.002	3.5
		272.50	.105	.001	.064	.002	4.2
		273.00	.098	.001	.057	.001	3.9
		273.50	.085	.001	.051	.001	4.7
		274.00	.072	.000	.046	.001	4.7
20.0	10.0	264.50	0.465	0.001	0.058	0.003	2.2
		265.00	.401	.002	.086	.004	1.9
		265.50	.354	.002	.092	.003	2.2
		266.00	.323	.001	.093	.002	2.0
		266.50	.290	.001	.100	.003	2.3
		267.00	.262	.001	.114	.001	1.8
		267.50	.242	.002	.110	.003	2.1
		268.00	.223	.002	.109	.003	2.1
		268.50	.202	.001	.116	.001	2.3
		269.00	.188	.002	.113	.003	2.3
		269.50	.172	.002	.115	.003	2.3
		270.00	.164	.003	.105	.003	2.9
		270.63	.146	.004	.101	.005	4.2
		271.25	.126	.003	.098	.004	3.0
		271.88	.117	.001	.092	.002	3.1
		272.50	.102	.005	.085	.005	4.7
20.0	50.0	263.75	0.574	0.001	0.040	0.002	1.8
		264.13	.506	.001	.061	.003	2.0
		264.50	.449	.001	.075	.002	1.8
		265.00	.393	.001	.089	.001	2.0
		265.50	.348	.001	.101	.002	1.9
		266.00	.313	.001	.106	.002	1.8
		266.50	.283	.001	.112	.002	1.8
		267.00	.258	.001	.115	.001	1.8
		267.50	.236	.001	.116	.001	2.0
		268.00	.215	.001	.117	.001	2.0
		268.50	.197	.001	.114	.002	1.9
		269.00	.181	.002	.112	.003	1.8
		269.50	.166	.001	.112	.001	2.1
		270.00	.156	.005	.102	.006	2.6
		270.75	.132	.001	.098	.001	2.6
		271.50	.117	.001	.092	.001	2.6
		272.25	.100	.001	.084	.001	2.9
		273.00	.084	.000	.077	.000	3.6
20.0	90.0	263.50	0.565	0.002	0.071	0.004	2.0
		264.00	.476	.001	.097	.002	2.0
		264.50	.419	.001	.091	.002	1.9
		265.00	.369	.002	.101	.003	1.9
		265.50	.327	.001	.113	.003	1.8

TABLE II.—Continued.

Axial position, Z, percent	Radial position, R, percent	Tangential position, θ, deg	Axial velocity ratio, V_z/V_{cr}	Standard deviation, σ/V_{cr}	Circumferential velocity ratio, V_θ/V_{cr}	Standard deviation, σ/V_{cr}	Turbulence intensty, Tu, percent
20.0	90.0	266.00	0.294	0.001	0.118	0.001	2.1
		266.50	.268	.003	.116	.005	2.3
		267.00	.244	.001	.118	.003	2.4
		267.50	.227	.003	.110	.004	3.0
		268.00	.208	.001	.113	.001	3.0
		268.50	.191	.001	.112	.001	3.1
		269.00	.176	.002	.110	.004	4.1
		269.50	.163	.002	.108	.003	4.2
		270.00	.148	.004	.102	.005	6.6
		270.75	.134	.003	.092	.003	5.8
		271.50	.123	.001	.083	.002	4.7
		272.25	.095	.002	.079	.002	6.7
		273.00	.078	.002	.075	.002	4.2
30.0	50.0	263.50	0.628	0.002	0.234	0.004	2.7
		264.00	.528	.001	.203	.002	2.2
		264.50	.457	.002	.190	.003	2.3
		265.00	.402	.001	.179	.001	2.1
		265.50	.355	.000	.172	.001	2.1
		266.00	.317	.001	.165	.002	2.2
		266.50	.283	.001	.163	.001	2.1
		267.00	.256	.001	.157	.002	1.9
		267.50	.233	.001	.152	.001	1.9
		268.00	.209	.001	.151	.001	1.9
		268.50	.192	.001	.143	.002	1.9
		269.00	.173	.001	.139	.001	2.0
		269.50	.158	.002	.133	.002	2.0
		270.00	.142	.003	.130	.003	2.4
		270.50	.130	.003	.120	.003	2.6
		271.00	.117	.002	.113	.002	2.5
		271.50	.104	.002	.111	.002	2.2
		272.00	.091	.001	.111	.001	2.6
40.0	10.0	263.50	0.532	0.002	0.424	0.003	2.2
		264.00	.480	.002	.357	.002	2.6
		264.50	.437	.001	.316	.001	2.6
		265.00	.403	.002	.269	.002	2.7
		265.50	.359	.002	.252	.002	2.7
		266.00	.323	.002	.235	.002	2.8
		266.50	.288	.002	.226	.002	2.5
		267.00	.264	.002	.210	.003	2.8
		267.50	.237	.002	.205	.002	2.7
		268.00	.217	.002	.191	.002	3.8
		268.50	.200	.003	.178	.003	3.1
		268.50	.194	.001	.185	.001	3.0
		269.00	.172	.002	.179	.002	2.6
		269.50	.156	.001	.167	.001	2.6
		270.00	.136	.002	.162	.002	2.5
		270.50	.120	.001	.156	.001	2.8
		271.00	.108	.002	.148	.003	2.4
40.0	50.0	262.95	0.579	0.004	0.487	0.005	2.6
		263.45	.543	.002	.388	.003	2.9
		263.95	.485	.002	.339	.002	2.7
		264.45	.435	.001	.296	.001	3.0
		264.95	.390	.002	.269	.003	2.9
		265.45	.350	.001	.247	.001	3.0

TABLE II.—Continued.

Axial position, Z, percent	Radial position, R, percent	Tangential position, θ, deg	Axial velocity ratio, V_z/V_{cr}	Standard deviation, σ/V_{cr}	Circumferential velocity ratio, V_θ/V_{cr}	Standard deviation, σ/V_{cr}	Turbulence intensty, Tu, percent
40.0	50.0	265.95	0.315	0.001	0.231	0.001	2.9
		266.45	.282	.001	.218	.002	3.0
		266.95	.253	.002	.210	.002	3.0
		267.45	.230	.002	.196	.002	3.2
		267.95	.206	.001	.186	.001	3.2
		268.45	.182	.001	.181	.001	2.9
		268.95	.167	.001	.171	.001	2.9
		269.45	.150	.001	.160	.001	3.0
		269.95	.132	.002	.156	.002	2.8
		270.45	.118	.003	.151	.003	2.9
		270.95	.109	.002	.135	.003	2.8
40.0	90.0	263.00	0.581	0.006	0.370	0.006	2.7
		263.50	.502	.002	.344	.002	2.5
		264.00	.455	.001	.307	.001	2.3
		264.50	.408	.003	.270	.004	2.6
		265.00	.371	.002	.238	.002	2.6
		265.50	.332	.001	.221	.001	2.6
		266.00	.299	.003	.215	.003	2.6
		266.50	.272	.003	.204	.004	3.1
		267.00	.249	.004	.189	.004	3.6
		267.50	.227	.002	.182	.003	4.2
		268.00	.216	.004	.162	.004	4.9
		268.00	.213	.003	.166	.004	5.2
		268.50	.194	.002	.160	.002	5.4
		269.00	.172	.003	.147	.004	5.8
		269.50	.153	.003	.145	.004	4.4
		270.00	.128	.001	.147	.001	3.5
		270.50	.109	.003	.149	.003	2.4
		271.00	.095	.003	.140	.003	2.8
50.0	50.0	262.00	0.475	0.012	0.619	0.010	3.0
		262.50	.493	.005	.562	.005	2.5
		263.00	.482	.005	.489	.005	3.0
		263.50	.443	.004	.441	.003	2.7
		264.00	.410	.002	.400	.002	2.6
		264.50	.377	.002	.363	.002	2.7
		265.00	.343	.003	.331	.002	2.6
		265.50	.310	.003	.306	.003	2.6
		266.00	.279	.002	.285	.002	2.4
		266.50	.252	.002	.267	.001	2.4
		267.00	.230	.002	.249	.002	2.5
		267.50	.204	.003	.238	.002	2.4
		268.00	.184	.001	.223	.001	2.7
		268.50	.161	.002	.213	.002	2.7
		269.00	.143	.001	.200	.001	2.6
		269.50	.130	.001	.183	.001	2.3
60.0	10.0	260.75	0.390	0.009	0.764	0.007	2.3
		261.25	.395	.005	.737	.004	2.3
		261.75	.393	.009	.695	.007	2.5
		262.25	.397	.006	.642	.005	2.7
		262.75	.409	.006	.577	.004	2.6
		263.25	.402	.005	.531	.004	2.4
		263.75	.378	.004	.495	.003	2.5
		264.25	.357	.002	.451	.001	2.4
		264.75	.331	.004	.417	.003	2.3

TABLE II.—Continued.

Axial position, Z, percent	Radial position, R, percent	Tangential position, θ, deg	Axial velocity ratio, V_z/V_{cr}	Standard deviation, σ/V_{cr}	Circumferential velocity ratio, V_θ/V_{cr}	Standard deviation, σ/V_{cr}	Turbulence intensty, Tu, percent
60.0	10.0	265.25	0.304	0.002	0.387	0.001	2.3
		265.75	.272	.002	.365	.002	2.2
		266.25	.248	.001	.340	.001	2.2
		266.75	.218	.002	.322	.002	1.9
		267.25	.196	.001	.301	.001	2.2
		267.75	.175	.002	.283	.001	2.0
60.0	50.0	260.30	0.392	0.015	0.757	0.011	4.3
		260.80	.408	.007	.737	.005	2.5
		261.30	.417	.005	.705	.004	2.8
		261.80	.422	.006	.664	.005	2.8
		262.30	.414	.005	.610	.004	3.0
		262.80	.405	.006	.565	.005	3.3
		263.30	.392	.006	.512	.004	3.4
		263.80	.370	.005	.471	.003	3.2
		264.30	.342	.003	.431	.002	3.2
		264.80	.318	.002	.396	.001	3.3
		265.30	.292	.001	.367	.001	3.3
		265.80	.267	.002	.343	.001	3.1
		266.30	.236	.002	.324	.002	3.1
		266.80	.216	.001	.301	.001	3.0
		267.30	.190	.002	.282	.001	2.7
60.0	90.0	260.25	0.378	0.006	0.747	0.004	2.8
		260.75	.398	.005	.712	.003	2.7
		261.25	.408	.004	.677	.003	2.9
		261.75	.413	.006	.627	.004	3.1
		262.25	.415	.007	.582	.005	3.1
		262.75	.406	.004	.534	.003	3.4
		263.25	.396	.007	.483	.005	3.2
		263.75	.378	.004	.438	.003	3.5
		264.25	.356	.004	.397	.003	3.3
		264.75	.328	.004	.370	.003	3.8
		265.25	.290	.004	.345	.003	3.2
		265.75	.271	.005	.321	.004	3.5
		266.25	.248	.002	.299	.002	3.8
		266.75	.216	.002	.288	.001	3.5
		267.25	.185	.004	.275	.003	2.8
		267.75	.161	.001	.256	.001	2.9
70.0	50.0	258.20	0.297	0.010	0.802	0.006	3.2
		258.70	.302	.008	.801	.004	2.5
		259.20	.316	.009	.783	.005	2.5
		259.70	.335	.009	.764	.005	2.7
		260.20	.349	.010	.741	.006	2.6
		260.70	.356	.006	.716	.003	2.7
		261.20	.355	.007	.685	.004	3.1
		261.70	.359	.004	.654	.003	2.9
		262.20	.352	.004	.617	.002	2.7
		262.70	.339	.004	.583	.002	2.6
		263.20	.329	.002	.543	.001	3.0
		263.70	.310	.003	.512	.002	2.5
		264.20	.295	.001	.478	.001	2.2
		264.70	.272	.002	.447	.001	3.6
		265.20	.255	.003	.413	.001	2.1
		265.70	.224	.003	.382	.002	2.6
		266.20	.192	.002	.363	.001	2.2

TABLE II.—Continued.

Axial position, Z, percent	Radial position, R, percent	Tangential position, θ, deg	Axial velocity ratio, V_z/V_{cr}	Standard deviation, σ/V_{cr}	Circumferential velocity ratio, V_θ/V_{cr}	Standard deviation, σ/V_{cr}	Turbulence intensty, Tu, percent
80.0	10.0	256.90	0.310	0.017	0.841	0.009	2.8
		257.35	.308	.015	.838	.008	3.0
		257.80	.323	.014	.827	.007	2.7
		258.25	.329	.014	.819	.007	2.8
		258.70	.350	.012	.797	.006	3.1
		259.10	.374	.011	.778	.005	2.9
		259.55	.375	.011	.770	.005	3.0
		260.00	.386	.006	.762	.003	2.8
		260.45	.383	.007	.745	.003	2.9
		260.90	.380	.010	.722	.005	3.4
		261.40	.370	.010	.698	.005	3.2
		261.90	.370	.010	.653	.005	3.1
		262.40	.331	.007	.642	.003	2.9
		262.90	.308	.003	.613	.002	2.8
		263.40	.288	.003	.583	.001	2.4
		263.90	.268	.004	.555	.002	2.2
		264.40	.247	.002	.529	.001	2.1
		264.90	.236	.006	.474	.003	3.0
80.0	10.0	256.90	0.313	0.018	0.840	0.009	5.1
		257.40	.318	.016	.839	.008	4.3
		257.90	.317	.015	.831	.008	4.7
		258.40	.339	.012	.813	.006	4.0
		258.90	.362	.009	.794	.004	4.1
		259.40	.386	.006	.773	.003	4.1
		259.90	.383	.005	.768	.002	3.6
		260.40	.392	.007	.746	.003	3.6
		260.90	.367	.006	.737	.003	4.1
		261.40	.372	.013	.705	.006	3.7
		261.90	.361	.012	.670	.006	3.7
		262.40	.334	.008	.643	.004	3.3
		262.90	.307	.004	.618	.002	3.3
		263.40	.290	.003	.589	.001	2.8
		263.90	.274	.004	.560	.002	2.8
		264.40	.252	.003	.532	.001	2.7
		264.90	.233	.004	.498	.002	3.0
80.0	50.0	256.60	0.256	0.020	0.787	0.010	10.4
		257.10	.284	.014	.816	.007	4.9
		257.60	.301	.011	.808	.006	4.6
		258.10	.307	.006	.799	.003	3.7
		258.60	.313	.008	.788	.004	3.8
		259.10	.330	.007	.770	.004	3.6
		259.60	.339	.008	.756	.004	3.7
		260.10	.344	.007	.737	.004	3.5
		260.60	.355	.008	.710	.004	3.9
		261.10	.349	.010	.688	.005	3.7
		261.60	.339	.010	.664	.005	3.8
		262.10	.324	.007	.639	.004	3.5
		262.60	.310	.004	.608	.002	3.1
		263.10	.297	.004	.579	.002	3.9
		263.60	.285	.003	.544	.001	2.6
		264.10	.253	.002	.519	.001	2.3
		264.60	.240	.006	.490	.003	2.5
		264.85	.243	.002	.478	.001	10.5

TABLE II.—Continued.

Axial position, Z, percent	Radial position, R, percent	Tangential position, θ, deg	Axial velocity ratio, V_z/V_{cr}	Standard deviation, σ/V_{cr}	Circumferential velocity ratio, V_θ/V_{cr}	Standard deviation, σ/V_{cr}	Turbulence intensty, Tu, percent
80.0	90.0	256.80	0.289	0.004	0.796	0.002	3.3
		257.30	.296	.005	.784	.003	3.4
		257.80	.290	.004	.779	.002	3.6
		258.30	.302	.006	.761	.003	4.0
		258.80	.323	.006	.743	.003	3.9
		259.30	.347	.008	.721	.004	4.2
		259.80	.354	.009	.708	.004	4.2
		260.30	.374	.005	.682	.002	4.2
		260.80	.375	.005	.664	.003	4.0
		261.30	.382	.007	.638	.003	4.4
		261.80	.379	.003	.615	.002	4.1
		262.30	.353	.006	.590	.003	3.7
		262.80	.330	.005	.566	.003	3.3
		263.30	.302	.004	.542	.002	3.0
		263.80	.281	.004	.509	.002	2.7
		264.30	.253	.003	.484	.001	2.5
		264.80	.235	.002	.457	.001	2.4
90.0	50.0	253.30	0.216	0.006	0.834	0.003	3.7
		253.80	.230	.005	.842	.003	3.0
		254.30	.233	.008	.844	.004	2.9
		254.80	.243	.005	.841	.002	2.9
		255.30	.247	.007	.837	.004	3.1
		255.80	.258	.004	.834	.002	3.0
		256.30	.259	.006	.829	.003	3.7
		256.80	.269	.008	.820	.004	2.7
		257.30	.276	.006	.808	.003	2.9
		257.80	.283	.006	.799	.003	3.1
		258.30	.282	.006	.792	.003	2.8
		258.80	.288	.007	.771	.004	2.8
		259.30	.292	.009	.753	.005	2.9
		259.80	.302	.009	.729	.005	2.9
		260.30	.304	.009	.710	.004	3.1
		260.80	.313	.008	.692	.004	3.0
		261.30	.320	.008	.679	.004	3.1
		261.80	.285	.009	.669	.005	2.8
		262.30	.286	.005	.643	.002	3.0
		262.80	.271	.004	.619	.002	2.6
100.0	50.0	250.50	0.192	0.006	0.813	0.003	3.1
		251.00	.206	.005	.823	.002	3.3
		251.50	.216	.006	.829	.003	3.5
		252.00	.221	.007	.833	.003	3.4
		252.50	.226	.004	.837	.002	3.1
		253.00	.235	.007	.837	.003	3.0
		253.50	.231	.009	.840	.004	2.8
		254.00	.249	.008	.839	.003	3.0
		254.50	.248	.006	.838	.003	2.8
		255.00	.253	.007	.837	.003	3.0
		255.50	.261	.006	.831	.003	3.2
		256.00	.269	.006	.825	.003	3.0
		256.50	.264	.004	.820	.002	2.9
		257.00	.271	.008	.815	.004	3.1
		257.50	.272	.004	.806	.002	3.0
		258.00	.284	.006	.794	.003	3.1
		258.50	.277	.004	.781	.002	3.3
		259.00	.276	.006	.769	.003	3.4
		259.50	.283	.007	.745	.003	3.9

TABLE II.—Continued.

Axial position, Z, percent	Radial position, R, percent	Tangential position, θ, deg	Axial velocity ratio, V_z/V_{cr}	Standard deviation, σ/V_{cr}	Circumferential velocity ratio, V_θ/V_{cr}	Standard deviation, σ/V_{cr}	Turbulence intensty, Tu, percent
100.0	50.0	260.00	0.275	0.005	0.722	0.002	3.5
		260.50	.275	.005	.689	.002	3.4
		261.00	.287	.004	.657	.002	4.9
105.0	50.0	247.50	0.156	0.007	0.719	0.003	3.0
		248.00	.170	.008	.770	.003	2.6
		248.50	.161	.007	.784	.003	3.2
		249.00	.172	.008	.786	.004	4.3
		249.50	.186	.008	.795	.003	2.9
		250.00	.198	.004	.802	.002	2.6
		250.50	.199	.003	.809	.001	2.6
		251.00	.204	.005	.825	.002	3.8
		251.50	.205	.008	.833	.003	4.3
		252.00	.230	.008	.828	.004	4.4
		252.50	.230	.009	.829	.004	3.1
		253.00	.237	.006	.831	.002	5.4
		253.50	.240	.008	.831	.003	4.9
		254.00	.243	.005	.838	.002	4.3
		254.50	.256	.011	.832	.005	6.9
		255.00	.252	.009	.822	.004	3.3
		255.50	.251	.007	.827	.003	3.2
		256.00	.244	.004	.826	.002	3.3
		256.50	.258	.004	.815	.002	3.4
		257.00	.256	.006	.812	.003	3.3
		257.50	.263	.008	.802	.003	3.5
		258.00	.266	.008	.790	.003	6.3
		258.50	.267	.004	.779	.002	3.3
		259.00	.266	.003	.766	.001	3.3
		259.25	.259	.009	.756	.004	3.7
		259.50	.267	.007	.742	.003	4.7
		259.75	.278	.006	.714	.003	5.9
		260.00	.262	.010	.656	.004	7.8
		260.25	.248	.006	.588	.003	8.5
		260.50	.233	.005	.538	.002	9.8
		260.75	.191	.013	.624	.006	9.5
		261.00	.177	.006	.681	.003	3.9
		261.25	.156	.005	.714	.002	3.1
		261.50	.159	.008	.749	.004	2.8
		261.75	.173	.005	.763	.002	2.9
		262.00	.178	.007	.777	.003	2.9
		262.50	.185	.008	.787	.004	2.7
		263.00	.197	.006	.788	.003	2.9
110.0	50.0	247.50	0.184	0.007	0.721	0.003	3.1
		248.00	.175	.007	.753	.003	2.8
		248.50	.184	.009	.771	.004	2.5
		249.00	.177	.012	.779	.005	3.1
		249.50	.180	.005	.786	.002	2.7
		250.00	.199	.006	.798	.003	2.7
		250.50	.190	.007	.802	.003	2.8
		251.00	.201	.002	.808	.001	2.9
		251.50	.205	.004	.818	.002	3.0
		252.00	.214	.006	.822	.003	2.7
		252.50	.217	.006	.823	.003	2.6
		253.00	.224	.005	.824	.002	2.8
		253.50	.226	.006	.826	.003	3.7
		254.00	.226	.005	.826	.002	2.9

TABLE II.—Continued.

Axial position, Z, percent	Radial position, R, percent	Tangential position, θ, deg	Axial velocity ratio, V_z/V_{cr}	Standard deviation, σ/V_{cr}	Circumferential velocity ratio, V_θ/V_{cr}	Standard deviation, σ/V_{cr}	Turbulence intensty, Tu, percent
110.0	50.0	254.50	0.236	0.005	0.825	0.002	2.9
		255.00	.252	.005	.819	.002	3.3
		255.50	.241	.005	.819	.002	3.0
		256.00	.258	.005	.813	.002	3.0
		256.50	.254	.008	.809	.003	3.0
		257.00	.249	.006	.806	.003	3.1
		257.50	.261	.006	.794	.002	3.0
		258.00	.271	.009	.778	.004	3.6
		258.50	.281	.014	.731	.006	5.8
		259.00	.261	.008	.645	.003	7.4
		259.50	.224	.020	.686	.009	7.4
		260.00	.236	.009	.731	.004	3.5
		260.50	.219	.008	.720	.004	2.7
		261.00	.194	.006	.715	.003	2.8
		261.50	.192	.009	.733	.004	2.9
		262.00	.177	.007	.761	.003	3.0
		262.50	.187	.005	.778	.002	3.0
		263.00	.197	.005	.780	.002	3.0
125.0	10.0	247.50	0.206	0.007	0.831	0.003	2.3
		248.00	.208	.007	.834	.003	2.2
		248.50	.208	.008	.841	.003	2.2
		249.00	.206	.012	.847	.005	2.1
		249.50	.208	.012	.850	.005	2.1
		250.00	.208	.011	.855	.005	2.5
		250.50	.203	.015	.855	.007	3.2
		251.00	.212	.018	.852	.008	3.0
		251.50	.232	.019	.851	.008	2.8
		252.50	.233	.016	.828	.007	4.4
		253.00	.206	.018	.826	.008	4.4
		253.50	.219	.012	.819	.005	4.9
		254.00	.222	.014	.815	.006	5.1
		254.50	.295	.020	.775	.009	6.1
		255.00	.195	.017	.830	.007	5.7
		255.50	.218	.026	.793	.011	7.0
		256.00	.282	.025	.784	.011	6.9
		256.50	.276	.015	.801	.007	5.9
		257.00	.276	.008	.821	.003	3.9
		257.50	.282	.010	.826	.004	3.0
		258.00	.285	.008	.819	.004	2.9
		258.50	.269	.009	.820	.004	3.0
		259.00	.273	.005	.809	.002	3.2
		259.50	.242	.004	.811	.002	3.0
		260.00	.236	.006	.812	.003	2.8
		260.50	.228	.005	.810	.002	2.5
		261.00	.220	.009	.819	.004	2.5
		261.50	.210	.006	.826	.003	2.3
		262.00	.216	.004	.829	.002	2.5
		262.50	.215	.006	.837	.002	3.9
		263.00	.209	.006	.843	.003	2.5
125.0	50.0	247.50	0.209	0.007	0.757	0.003	3.6
		248.00	.206	.004	.768	.002	3.9
		248.50	.206	.007	.781	.003	2.7
		249.00	.199	.006	.793	.003	2.8
		249.50	.205	.006	.799	.003	2.9

TABLE II.—Continued.

Axial position, Z, percent	Radial position, R, percent	Tangential position, θ, deg	Axial velocity ratio, V_z/V_{cr}	Standard deviation, σ/V_{cr}	Circumferential velocity ratio, V_θ/V_{cr}	Standard deviation, σ/V_{cr}	Turbulence intensty, Tu, percent
125.0	50.0	250.00	0.203	0.005	0.798	0.002	3.5
		250.50	.210	.003	.806	.001	2.7
		251.00	.211	.005	.811	.002	2.8
		251.50	.215	.005	.815	.002	2.9
		252.00	.215	.004	.823	.002	2.9
		252.50	.224	.005	.823	.002	3.2
		253.00	.229	.007	.819	.003	3.6
		253.50	.230	.010	.812	.004	4.1
		254.00	.238	.013	.794	.005	4.6
		254.50	.235	.013	.774	.006	5.2
		255.00	.228	.006	.771	.003	4.8
		255.50	.242	.007	.784	.003	4.8
		256.00	.252	.012	.802	.005	3.7
		256.50	.253	.004	.814	.002	3.5
		257.00	.254	.010	.809	.004	3.5
		257.50	.251	.010	.803	.004	3.5
		258.00	.248	.013	.792	.006	3.3
		258.50	.255	.007	.785	.003	3.8
		259.00	.254	.008	.777	.003	3.7
		259.50	.257	.005	.771	.002	3.9
		260.00	.248	.008	.760	.003	3.8
		260.50	.236	.005	.754	.002	3.5
		261.00	.222	.006	.760	.002	3.6
		261.50	.217	.011	.761	.005	3.7
		262.00	.209	.006	.770	.003	3.6
		262.50	.210	.005	.780	.002	4.0
125.0	90.0	247.50	0.268	0.007	0.688	0.003	4.9
		248.00	.253	.008	.694	.003	4.6
		248.50	.233	.010	.708	.005	4.5
		249.00	.238	.004	.719	.002	4.5
		249.50	.228	.011	.725	.005	3.6
		250.00	.208	.011	.744	.005	3.6
		250.50	.223	.011	.748	.005	3.3
		251.00	.217	.013	.753	.006	3.3
		251.50	.226	.004	.759	.002	6.1
		252.00	.227	.009	.764	.004	3.3
		252.50	.220	.004	.769	.002	3.2
		253.00	.226	.009	.775	.004	5.8
		253.50	.228	.009	.776	.004	3.4
		254.00	.221	.011	.778	.005	3.4
		254.50	.231	.010	.778	.004	3.7
		255.00	.247	.004	.767	.002	6.5
		255.50	.247	.012	.754	.005	5.5
		256.00	.245	.012	.715	.005	6.5
		256.50	.234	.011	.715	.005	6.0
		257.00	.260	.007	.716	.003	8.1
		257.50	.243	.010	.741	.004	4.6
		258.00	.245	.008	.744	.003	4.1
		258.50	.262	.005	.735	.002	4.3
		259.00	.278	.005	.725	.002	4.5
		259.50	.280	.009	.712	.004	4.8
		260.00	.293	.004	.700	.002	5.1
		260.50	.282	.005	.696	.002	5.0
		261.00	.277	.006	.688	.003	5.0
		261.50	.262	.006	.691	.003	4.8
		262.00	.236	.008	.699	.003	4.7

TABLE II.—Continued.

Axial position, Z, percent	Radial position, R, percent	Tangential position, θ, deg	Axial velocity ratio, V_z/V_{cr}	Standard deviation, σ/V_{cr}	Circumferential velocity ratio, V_θ/V_{cr}	Standard deviation, σ/V_{cr}	Turbulence intensty, Tu, percent
125.0	90.0	262.50	0.232	0.005	0.711	0.002	4.3
		263.00	.218	.004	.725	.002	3.9
150.0	50.0	247.50	0.207	0.008	0.742	0.004	4.1
		248.00	.201	.007	.759	.003	4.0
		248.50	.209	.006	.769	.003	3.4
		249.00	.216	.009	.779	.004	2.8
		249.50	.213	.007	.783	.003	2.6
		250.00	.213	.004	.789	.002	2.4
		250.50	.228	.009	.786	.004	2.5
		251.00	.220	.004	.794	.002	2.5
		251.50	.219	.006	.799	.003	2.4
		252.00	.219	.005	.800	.002	2.5
		252.50	.229	.003	.800	.001	2.7
		253.00	.227	.007	.806	.003	2.7
		253.50	.229	.005	.803	.002	2.7
		254.00	.241	.007	.802	.003	2.7
		254.50	.229	.004	.807	.002	2.7
		255.00	.236	.003	.805	.001	2.8
		255.50	.234	.007	.805	.003	2.7
		256.00	.238	.006	.804	.003	2.6
		256.50	.238	.005	.801	.002	2.7
		257.00	.243	.006	.799	.003	2.9
		257.50	.237	.006	.793	.003	2.9
		258.00	.236	.007	.785	.003	3.2
		258.50	.240	.007	.776	.003	3.6
		259.00	.214	.013	.757	.006	4.5
		259.50	.208	.011	.740	.005	4.6
		260.00	.211	.012	.726	.005	4.7
		260.50	.199	.009	.721	.004	4.9
		261.00	.193	.020	.716	.009	7.0
		261.50	.188	.007	.748	.003	5.3
		262.00	.207	.008	.765	.003	4.3
		262.50	.213	.011	.778	.005	3.2
175.0	50.0	247.50	0.228	0.004	0.776	0.002	3.2
		248.00	.223	.007	.777	.003	3.0
		248.50	.237	.009	.773	.004	2.9
		249.00	.222	.009	.781	.004	2.7
		249.50	.231	.008	.781	.004	3.0
		250.00	.223	.010	.779	.004	2.9
		250.50	.212	.009	.778	.004	3.2
		251.00	.219	.006	.776	.003	3.2
		251.50	.215	.014	.771	.006	3.4
		252.00	.213	.009	.765	.004	3.8
		252.50	.200	.006	.766	.003	4.0
		253.00	.201	.011	.768	.005	3.8
		253.50	.205	.011	.773	.005	3.9
		254.00	.213	.015	.775	.006	3.9
		254.50	.234	.013	.784	.006	3.3
		255.00	.217	.012	.792	.005	3.2
		255.50	.229	.005	.789	.002	3.5
		256.00	.231	.013	.791	.006	3.2
		256.50	.235	.005	.792	.002	2.7
		257.00	.242	.008	.791	.004	2.7
		257.50	.236	.006	.790	.003	2.9
		258.00	.225	.006	.795	.003	2.9

TABLE II.—Concluded.

Axial position, Z, percent	Radial position, R, percent	Tangential position, θ, deg	Axial velocity ratio, V_z/V_{cr}	Standard deviation, σ/V_{cr}	Circumferential velocity ratio, V_θ/V_{cr}	Standard deviation, σ/V_{cr}	Turbulence intensty, Tu, percent
175.0	50.0	258.50	0.238	0.011	0.784	0.005	2.9
		259.00	.238	.008	.782	.003	2.6
		259.50	.235	.010	.779	.004	3.1
		260.00	.231	.008	.784	.004	2.8
		260.50	.238	.010	.779	.005	2.6
		261.00	.222	.007	.779	.003	2.8
		261.50	.235	.009	.779	.004	2.5
		262.00	.223	.010	.780	.004	2.7
		262.50	.228	.009	.779	.004	2.7
		263.00	.223	.008	.780	.004	2.8
200.0	50.0	248.00	0.219	0.011	0.779	0.005	3.7
		248.75	.215	.012	.783	.005	3.0
		249.50	.217	.007	.785	.003	3.0
		250.25	.234	.013	.786	.006	2.8
		251.00	.221	.008	.787	.003	2.9
		251.75	.223	.009	.788	.004	2.7
		252.50	.237	.007	.785	.003	2.9
		253.25	.235	.008	.790	.003	2.9
		254.00	.229	.008	.791	.004	3.0
		254.75	.228	.011	.789	.005	3.3
		255.50	.224	.013	.786	.006	3.2
		256.25	.232	.009	.783	.004	3.3
		257.00	.216	.007	.774	.003	4.1
		257.75	.204	.011	.767	.005	4.2
		258.50	.210	.014	.763	.006	4.1
		259.25	.194	.008	.773	.003	4.2
		260.00	.202	.012	.775	.005	4.1
		260.75	.199	.010	.785	.005	3.8
		261.50	.211	.005	.784	.002	3.9
		262.25	.215	.010	.786	.004	3.6
		263.00	.211	.007	.783	.003	3.8

TABLE III.—VANE SUCTION AND PRESSURE SURFACE CIRCUMFERENTIAL LOCATIONS FOR HIGH TUNING TURBINE STATOR

Axial position, Z, percent	Radial position, R, percent	Suction surface location, θ_{ss}, deg	Pressure surface location, θ_{ps}, deg
0.0	50.0	262.28	276.13
10.0	50.0	263.42	274.77
20.0	10.0	263.94	274.15
	50.0	263.51	273.96
	90.0	263.14	273.79
30.0	50.0	263.25	272.90
40.0	10.0	263.02	271.79
	50.0	262.66	271.75
	90.0	262.34	271.73
50.0	50.0	261.59	270.40
60.0	10.0	260.15	268.68
	50.0	259.97	268.85
	90.0	259.82	269.01
70.0	50.0	257.85	267.37
80.0	10.0	255.09	265.05
	50.0	255.29	265.50
	90.0	255.36	265.80
90.0	50.0	251.96	263.47
100.0	50.0	248.22	262.07

15) are plotted on these figures as 2σ confidence intervals. If a confidence interval is not shown for a given point, the 2σ value fell within or close to the symbol used to represent the data and was not plotted to avoid confusion in the figures. All the 2σ confidence intervals are given in table II. Also shown on these figures are the theoretical results obtained from Denton's inviscid flow analysis program.

Upstream Measurements

The results upstream of the vane leading edge are shown in figures 10 to 13. The projection of the vane leading edge to the survey plane, shown in these figures, was calculated using the design inlet flow angle of 0°. In figures 10 to 12, for axial positions between −100 to −50 percent axial chord, the measurements are compared to the design value since Denton's calculation domain did not extend this far upstream. At these locations the measurements indicate a very uniform, axial, inlet velocity. Comparisons of the measurements and the design value are excellent. It can be noted that at −50 percent axial chord (fig. 12) a very slight influence of the vane leading edge appears. At −25 percent axial chord (fig. 13), the influence of the leading edge on the measurements is clearly evident. Comparisons of data and theoretical calculations are also very good to excellent at this position.

Passage Measurements

Measurements within the vane passage were made at every 10 percent of axial chord from the vane leading edge to the vane trailing edge, and these results are shown in figures 14

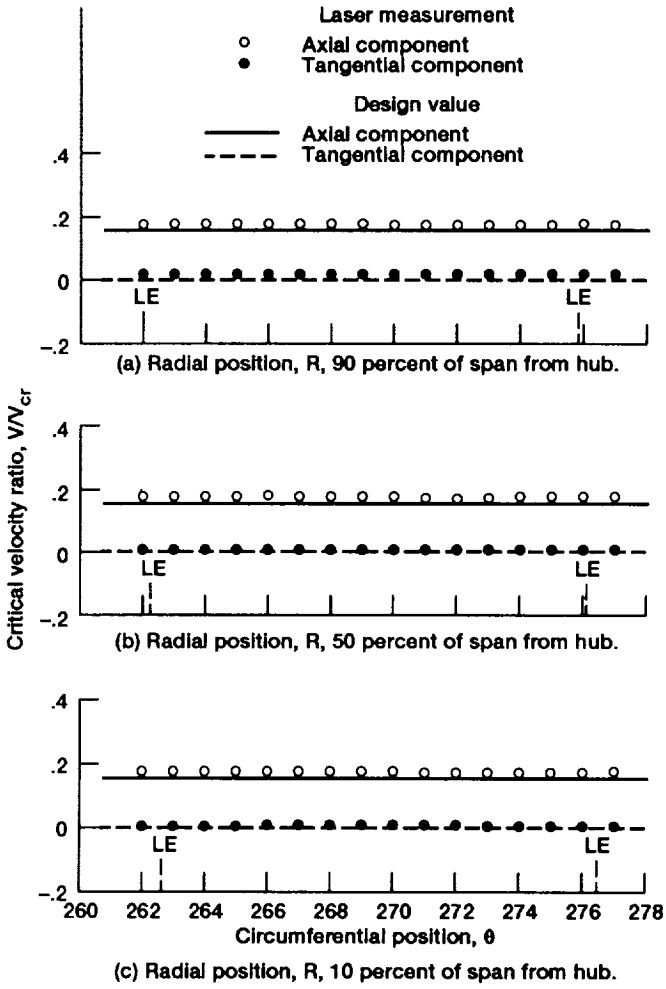

Figure 10.—Comparison of laser measurements and theory at −100-percent axial chord.

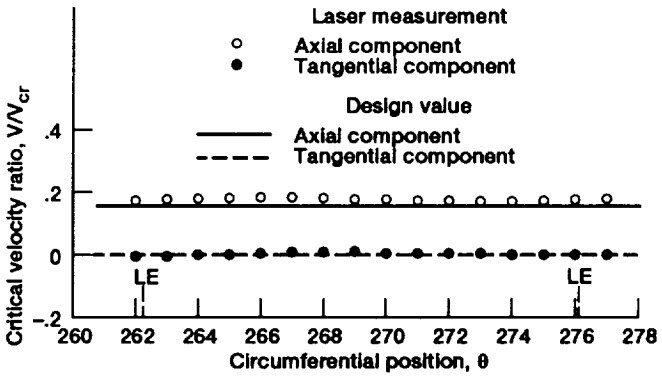

Figure 11.—Comparison of laser measurements and theory at −75-percent axial chord and 50-percent span.

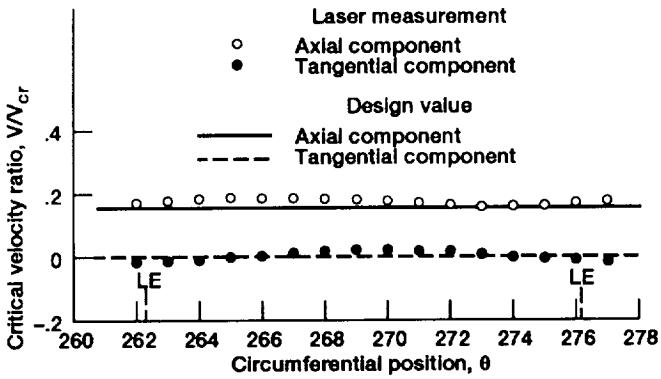

Figure 12.—Comparison of laser measurements and theory at -50-percent axial chord and 50-percent span.

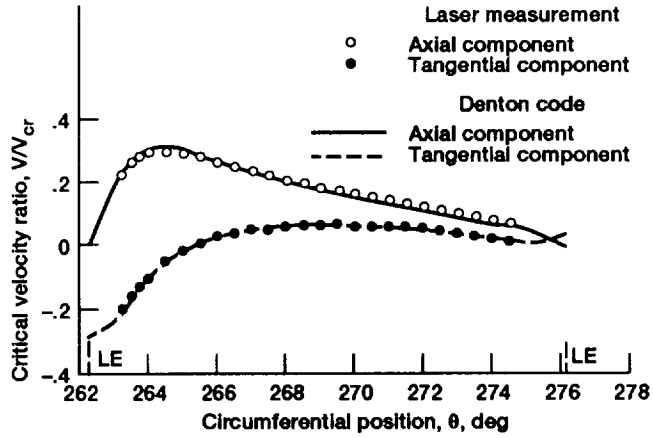

Figure 14.—Comparison of laser measurements and theory at 0-percent axial chord and 50-percent span.

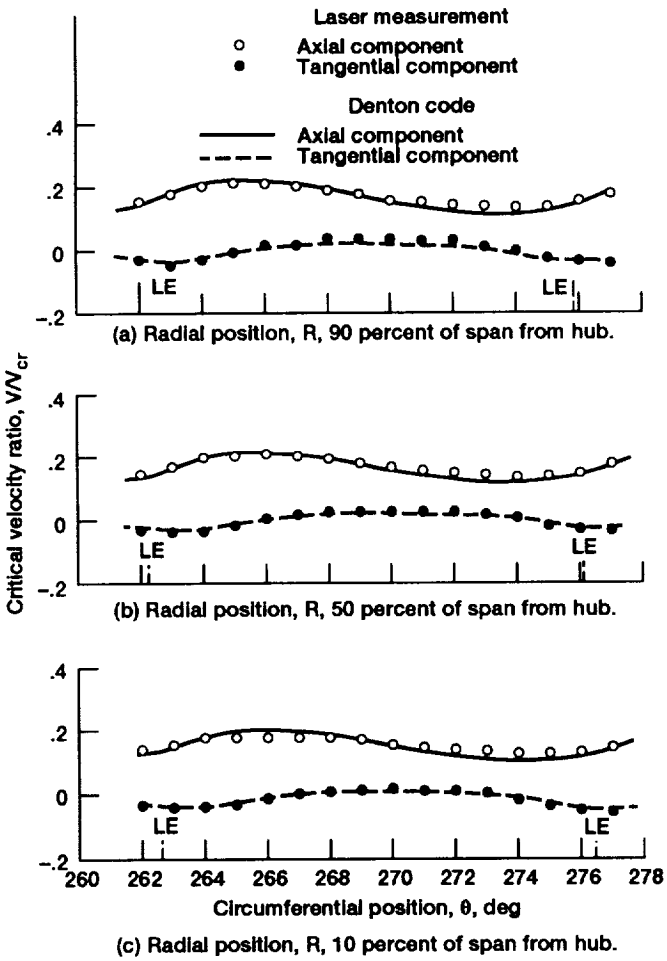

Figure 13.—Comparison of laser measurements and theory at -25-percent axial chord.

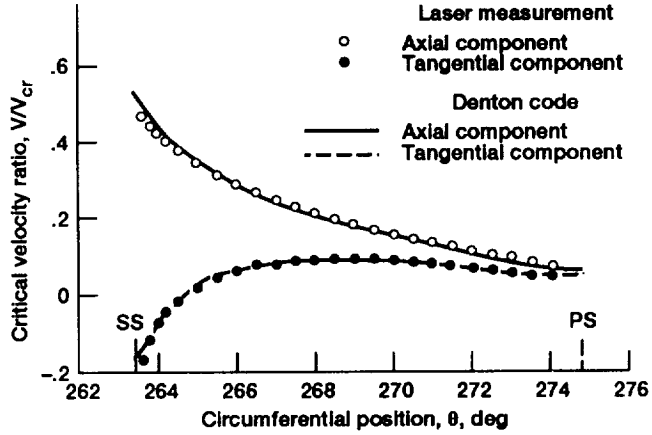

Figure 15.—Comparison of laser measurements and theory at 10-percent axial chord and 50-percent span.

to 24. For discussion purposes, the passage has been arbitrarily divided into leading-edge, midpassage, and trailing-edge regions.

Region near vane leading edge.—For positions of 0- to 30-percent axial chord (figs. 14 to 17), there are substaintial velocity changes occurring from suction side to pressure side of the passage caused by the large flow turning in the leading-edge region. In general, there is very good to excellent agreement between the measurements and Denton's calculations. However, at 10-percent axial chord the measured axial component near the suction surface is lower than Denton's calculations. Similarly, at 30-percent axial chord the measured tangential component near the suction surface is lower than the calculations. This is in agreement with the particle dynamics calculation, which indicated the possibility of some seed particle lag in these regions (see fig. 8).

Region near vane midpassage.—At positions of 40- to 60-percent axial chord (figs. 18 to 20), the comparisons of the measurements and the calculations are still very good.

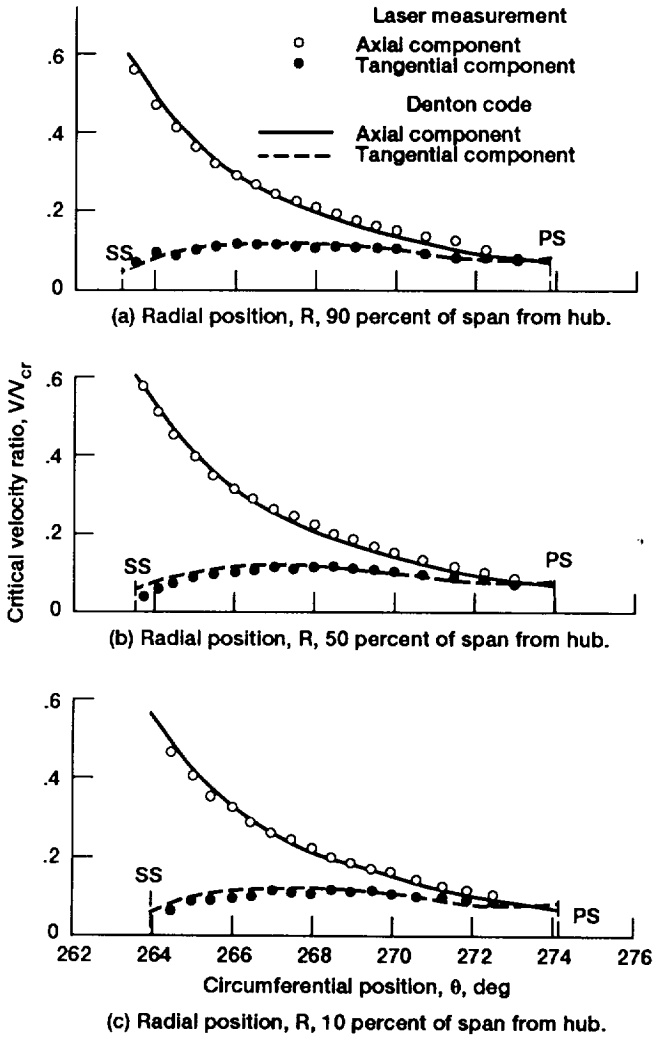

(a) Radial position, R, 90 percent of span from hub.

(b) Radial position, R, 50 percent of span from hub.

(c) Radial position, R, 10 percent of span from hub.

Figure 16.—Comparison of laser measurements and theory at 20-percent axial chord.

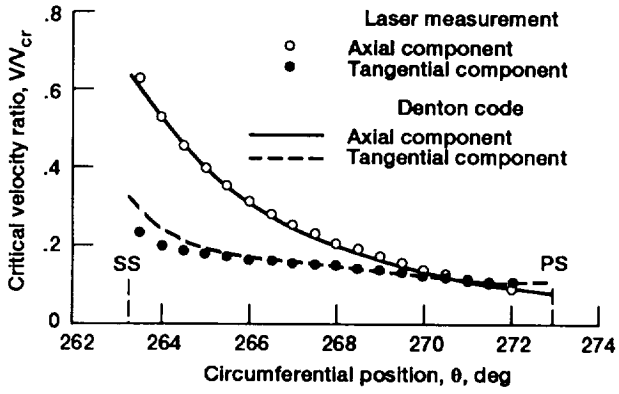

Figure 17.—Comparison of laser measurements and theory at 30-percent axial chord and 50-percent span.

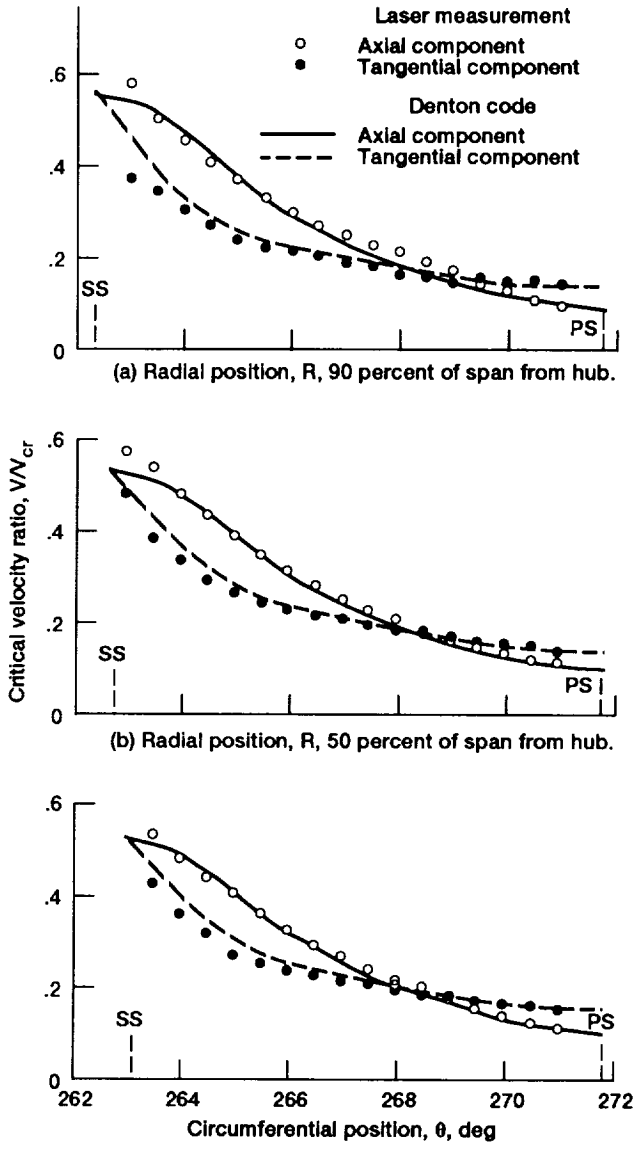

(a) Radial position, R, 90 percent of span from hub.

(b) Radial position, R, 50 percent of span from hub.

(c) Radial position, R, 10 percent of span from hub.

Figure 18.—Comparison of laser measurements and theory at 40-percent axial chord.

However, near the suction surface, the measured axial component is somewhat higher than the calculations. This was also predicted by the seed particle dynamics calculation (fig. 8).

Region near vane trailing edge.—For positions of 70- to 100-percent axial chord (figs.21 to 24), the flow turning results in tangential velocity components that are larger than the axial velocity components. At 80-percent axial chord (fig. 22), many statistical uncertainty bars appear in the figures. In addition, the trends in the measurements across the vane passage are not as smooth as in previous survey locations. As a check,

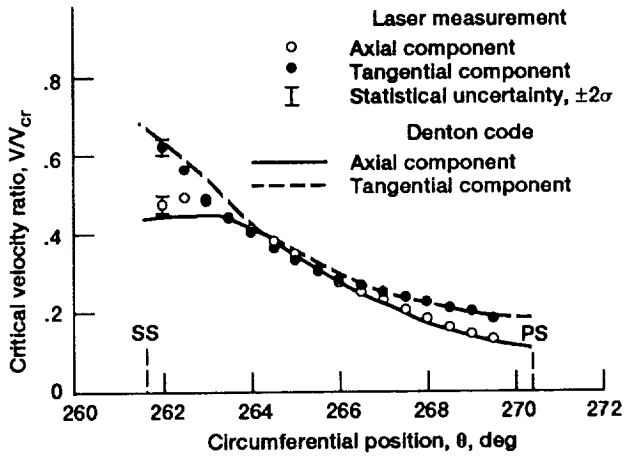

Figure 19.—Comparison of laser measurements and theory at 50-percent axial chord and 50-percent span.

two sets of measurements at 80-percent axial chord and 10-percent span were taken about 3 weeks apart and are shown in figures 22(c) and 22(d). The similar trends noted in both sets of data indicate their repeatability. One possible cause for the observed behavior would be a window imperfection at this particular axial location. While some of the largest differences between the measurements and calculations occur here, the agreement is still considered to be reasonable. It can also be noted at this location that at midpassage the measured tangential component is lower while the measured axial component is higher than the calculations. This tends to result in the velocity magnitude being closer to the calculated value while the flow turning is less than predicted. At 90- and 100-percent axial chord (figs. 23 and 24) the agreement between measurements and theory is quite good.

Downstream Measurements

The results downstream of the vane trailing edge are shown in figures 25 to 30. The projection of the vane trailing edge to the survey plane, shown in these figures, was calculated using the design exit flow angle of 75°. At 105-percent axial chord (fig. 25), the wake from the vane is clearly defined in the tangential component measurements. Outside the viscous region, the comparison is very good between the measurements and the inviscid calculations. As the flow proceeds downstream, the wake mixes out and can be less clearly delineated, but it is still present at 150-percent axial chord (fig. 28). Since the calculation domain did not extend to the 150-percent axial chord location, comparisons are made, thereafter, with the vane design value, which compares favorably. At 175- and 200-percent axial chord (figs. 29 and 30), the flow is more uniform but still has not completely mixed out.

Turbulence Measurements

The turbulence intensity at each measurement point is presented in table II. These values were obtained from the LA

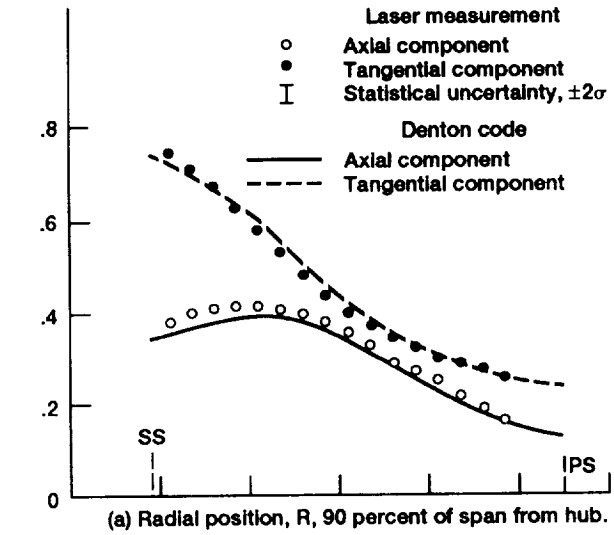

(a) Radial position, R, 90 percent of span from hub.

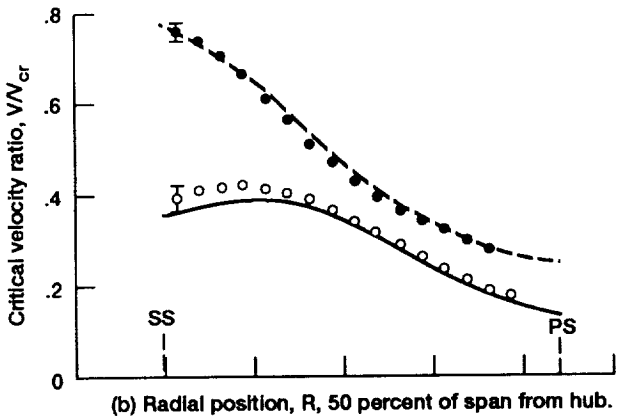

(b) Radial position, R, 50 percent of span from hub.

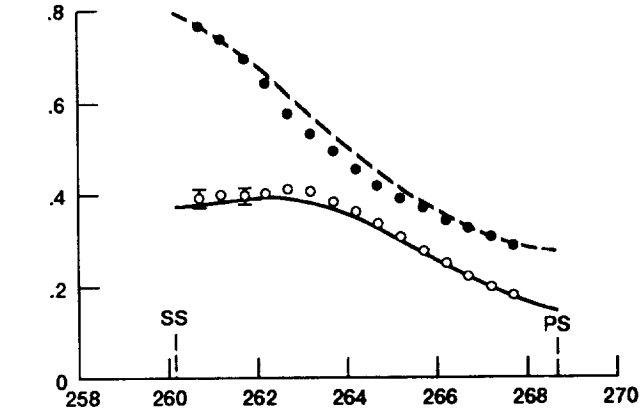

(c) Radial position, R, 10 percent of span from hub.

Figure 20.—Comparison of laser measurements and theory at 60-percent axial chord.

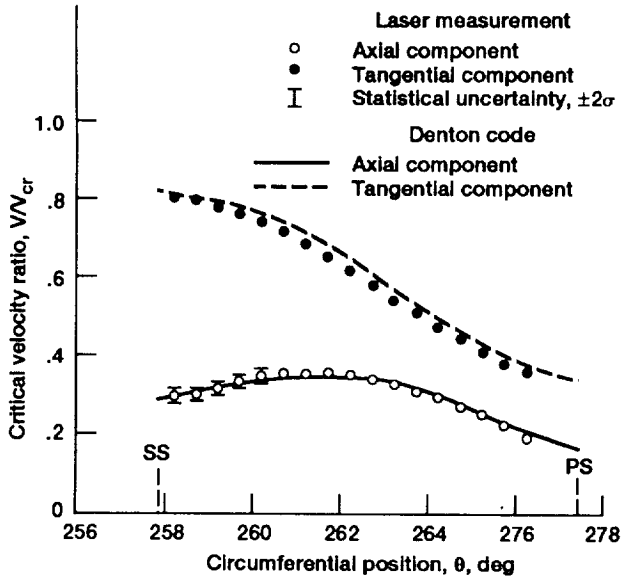

Figure 21.—Comparison of laser measurements and theory at 70-percent axial chord and 50-percent span.

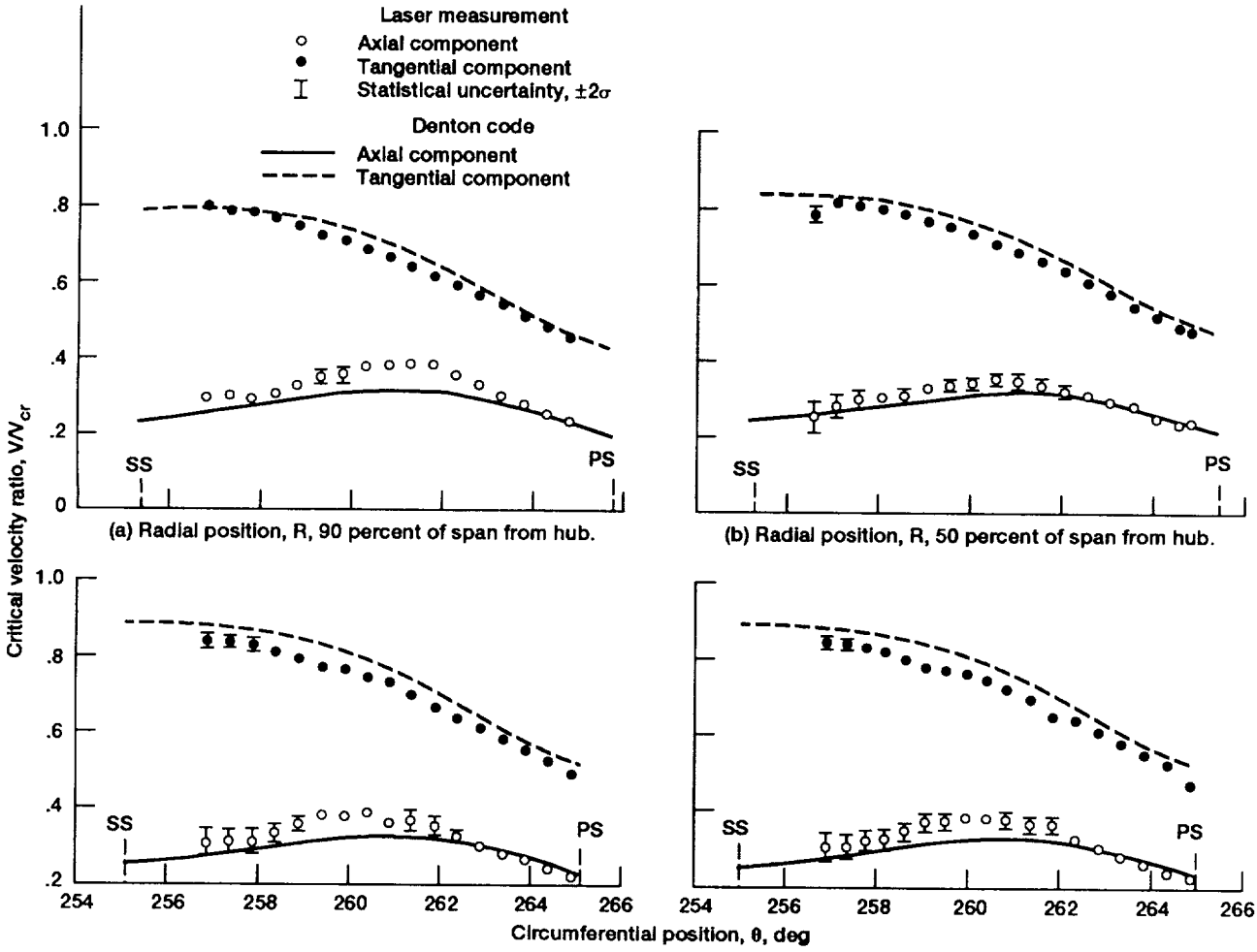

(a) Radial position, R, 90 percent of span from hub.

(b) Radial position, R, 50 percent of span from hub.

(c) Radial position, R, 10 percent of span from hub (repeatability check).

(d) Radial position, R, 10 percent of span from hub.

Figure 22.—Comparison of laser measurements and theory at 80-percent axial chord.

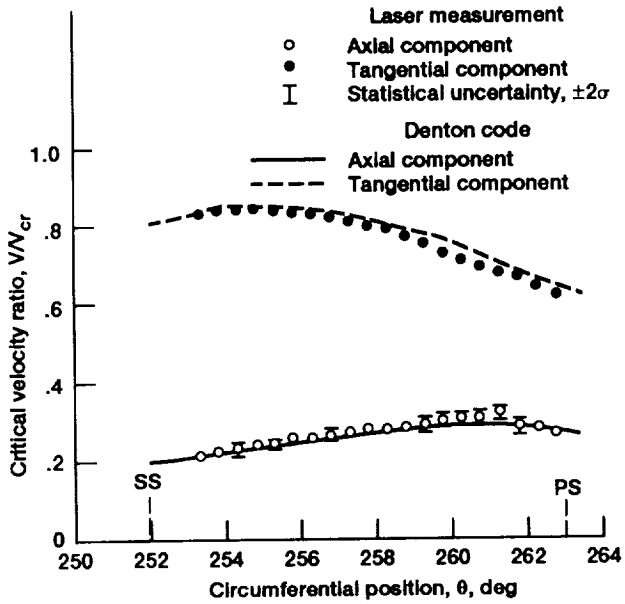

Figure 23.—Comparison of laser measurements and theory at 90-percent axial chord and 50-percent span.

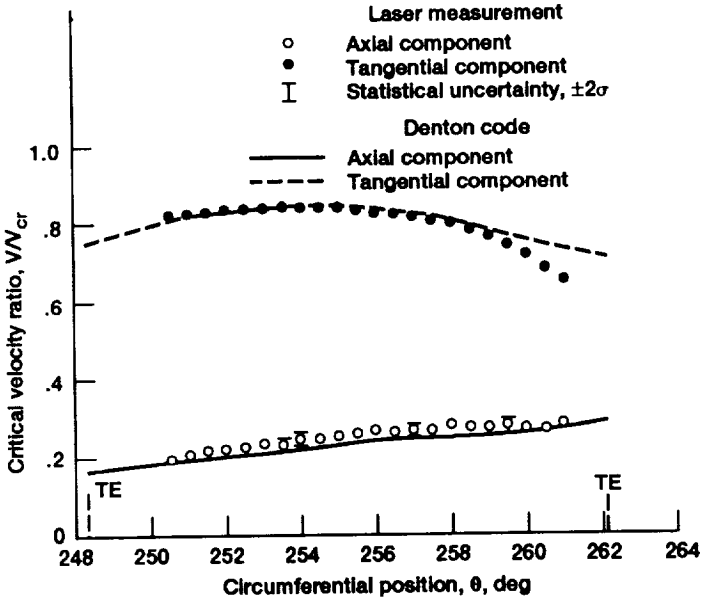

Figure 24.—Comparison of laser measurements and theory at 100-percent axial chord and 50-percent span.

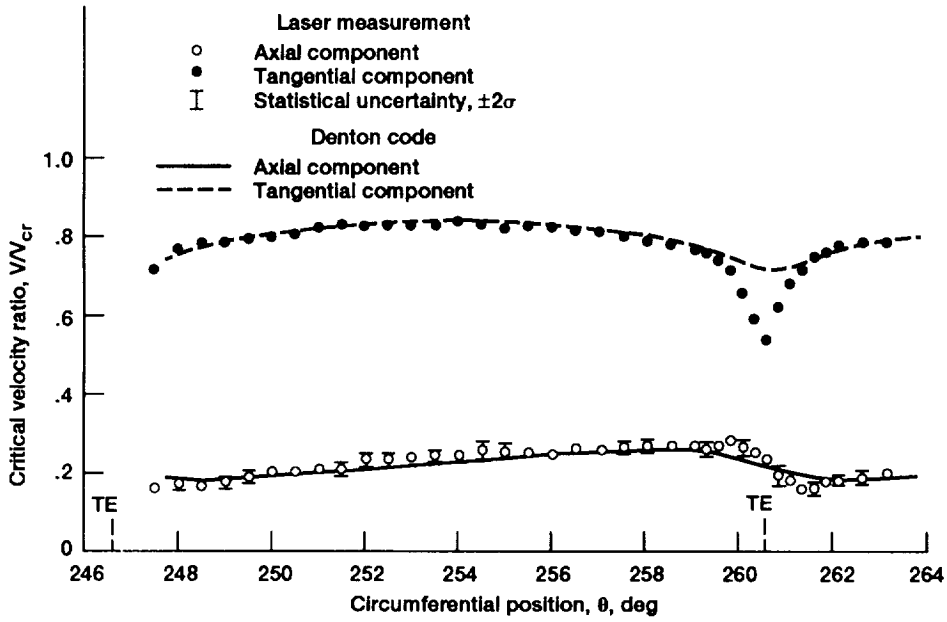

Figure 25.—Comparison of laser measurements and theory at 105-percent axial chord and 50-percent span.

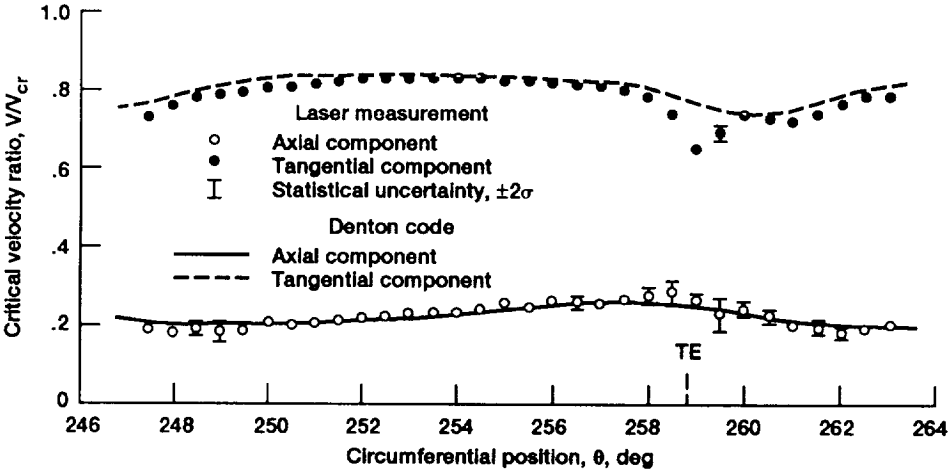

Figure 26.—Comparison of laser measurements and theory at 110-percent axial chord and 50-percent span.

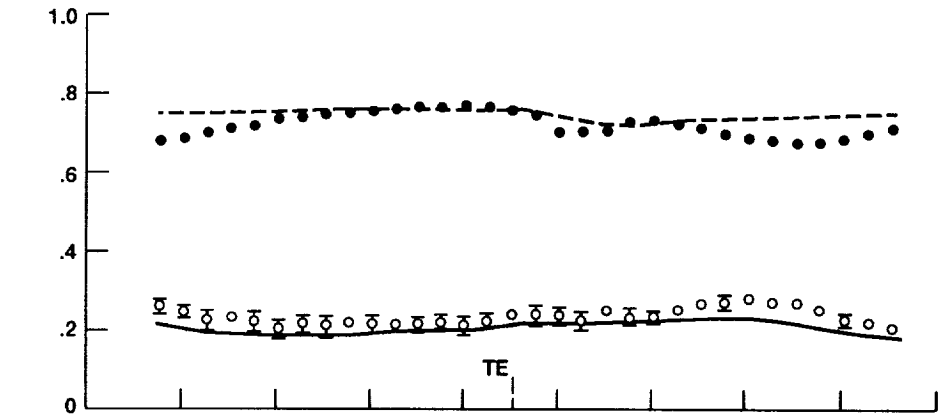

(a) Radial position, R, 90 percent of span from hub.

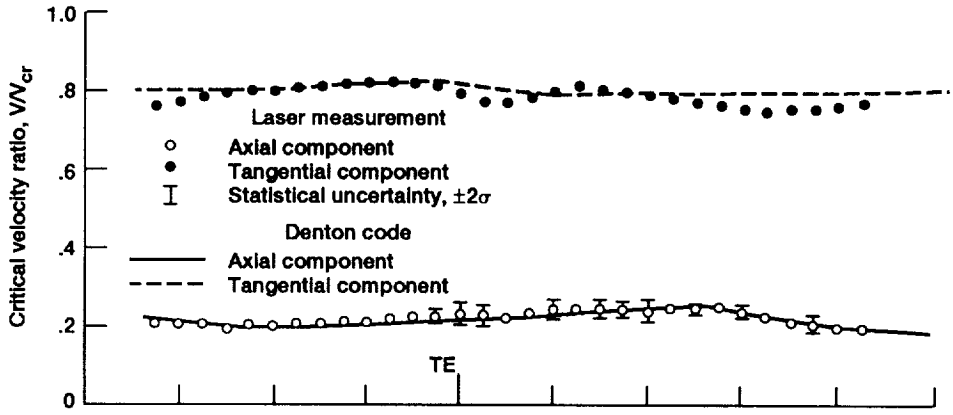

(b) Radial position, R, 50 percent of span from hub.

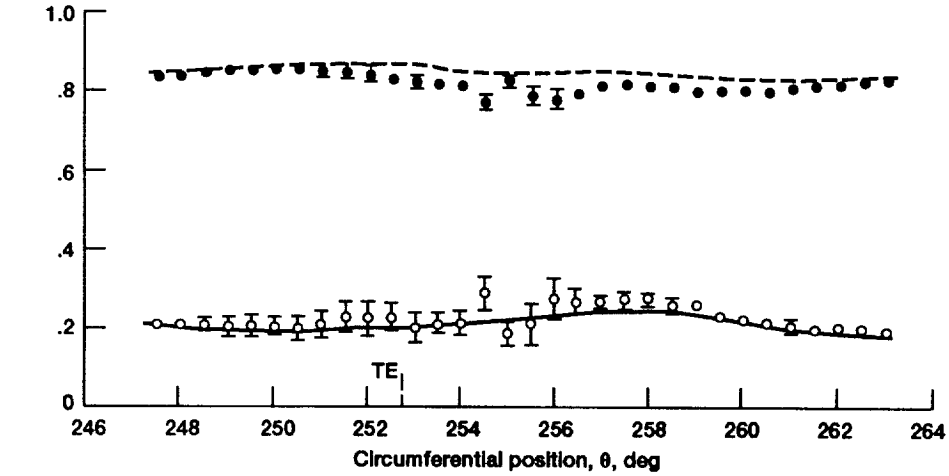

(c) Radial position, R, 10 percent of span from hub.

Figure 27.—Comparison of laser measurements and theory at 125-percent axial chord.

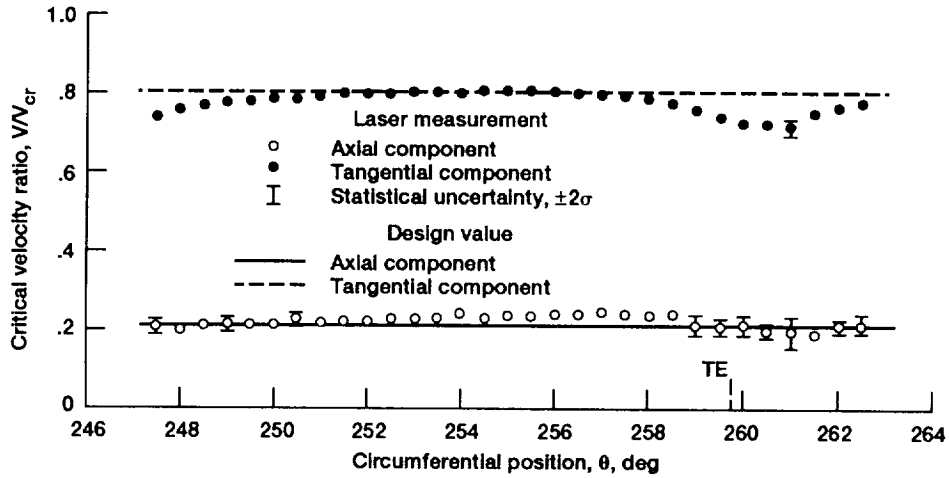

Figure 28.—Comparison of laser measurements and theory at 150-percent axial chord and 50-percent span.

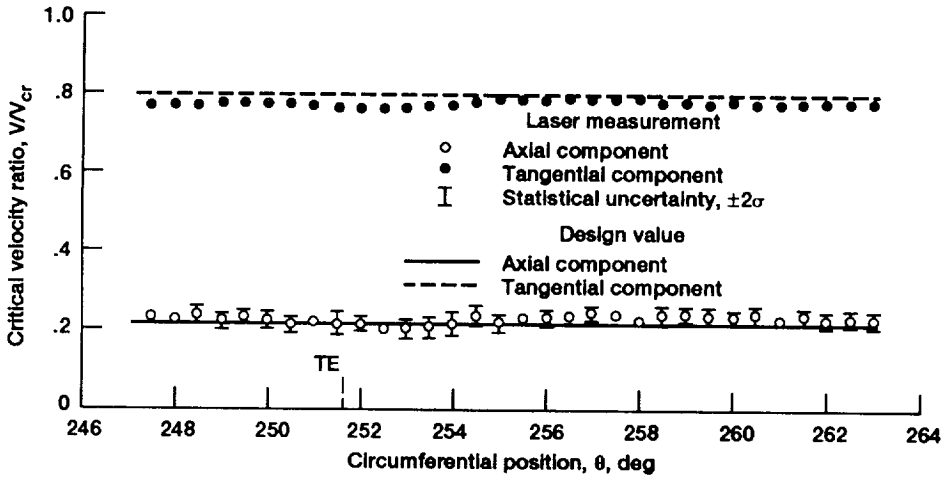

Figure 29.—Comparison of laser measurements and theory at 175-percent axial chord and 50-percent span.

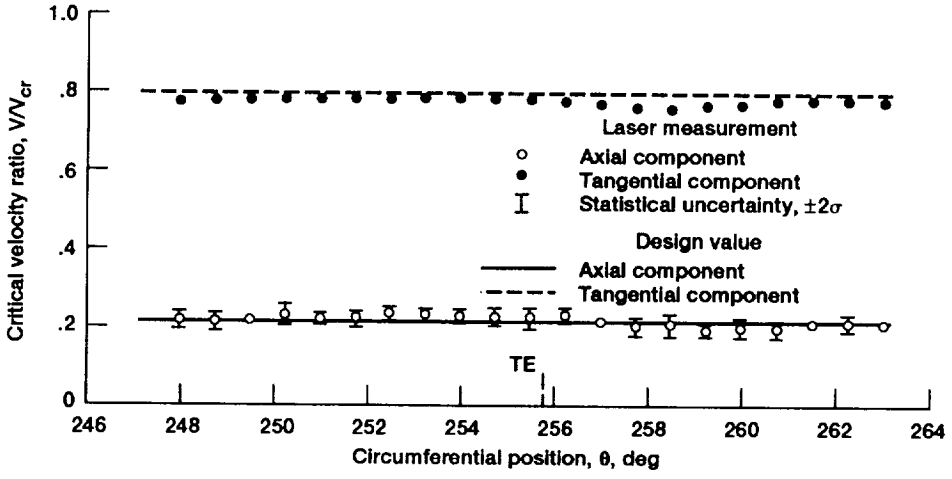

Figure 30.—Comparison of laser measurements and theory at 200-percent axial chord and 50-percent span.

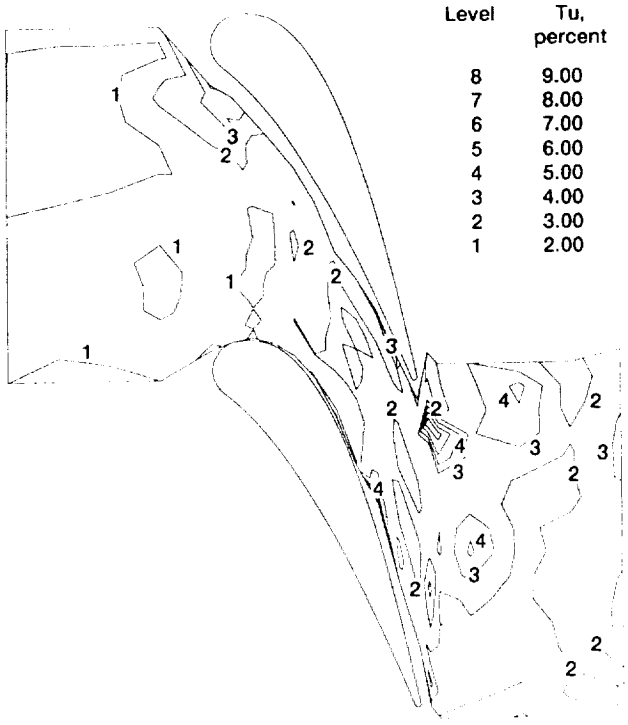

Figure 31.—Turbulence intensity Tu through vane passage at mean radius.

measurements assuming isotropic turbulence and no laser noise, as described in the **Calculation Procedures** section. Contours of turbulence intensity are shown in figure 31 for measurements taken at the mean radius. The turbulence intensity can be seen to increase as the flow passes through the vane passage. In general, the turbulence level varies from about 2 to 3 percent upstream of the vanes, to 3 to 4 percent in the vane passage, to 4 to 6 percent downstream of the vanes. Within the vane wakes, the turbulence levels are higher, about 7 to 9 percent. Similar turbulence levels were measured and reported previously for 67° flow turning vanes tested in this cascade with both cylindrical and contoured endwalls (refs. 10 and 11).

Summary of Results

An advanced laser anemometer (LA) was used to measure the mean axial and tangential velocity components in an annular cascade of turbine stator vanes designed for a high bypass ratio engine. These vanes were based on a redesign of the first-stage stator, of a two-stage turbine, that produced 75° of flow turning. Tests were conducted on a 0.771 scale model of the engine size stator. The advanced LA fringe system was designed to employ thinner than usual laser beams resulting in a 50-μm-diameter probe volume (PV). In comparison, this PV was half as large as in the configurations previously used in this cascade. This smaller size allowed the laser power to be more concentrated in the probe volume permitting measurements to be obtained from smaller seed particles and closer to surfaces. To prevent the beams from uncrossing in passing through the curved optical access window, beam correction optics were employed. In addition, the access window was manufactured to the same high quality as the other optical components used in the LA system.

An experimental measurement of the seed particle size distribution was obtained at the bellmouth entrance. A particle dynamics calculation was then performed for this vane geometry to determine how well seed particles of different sizes tracked the airflow. Experimental LA measurements of velocity and turbulence were obtained both upstream, within, and downstream of the stator vane row at the design exit critical velocity ratio of 0.896 at the hub. Surface static pressure measurements were also obtained near the vane hub, at midspan, and near the tip. The measurements were compared, where possible, with the results from Denton's three-dimensional inviscid flow analysis program. The data are presented in both graphic and tabulated form so that they may be readily used to compare against other turbomachinery computations. The results of this investigation are summarized as follows:

(1) Seed particles of 0.5-μm diameter, which are representative of the bulk of the aerosol generated by the seeder, follow the flow to within ± 0.5 percent (of critical velocity ratio) in both the axial and tangential velocity components. Seed particles of 1-μm diameter, which are near the upper end of the seed particle distribution, generally, follow the flow to within ± 1 percent (of critical velocity ratio) in both velocity components. However, differences of -2 percent in the tangential velocity component were indicated close to the suction surface of the vanes near the leading-edge region.

(2) The experimental measurements of vane surface static pressures compared well with the calculated values. The agreement was also, in general, quite good for the velocity component measurements. However, at midspan and near the vane tip, the measurements indicate slightly more vane loading over most of the surface than do the calculations.

(3) Upstream of the vanes (-100- to -50-percent axial chord) the laser anemometer measurements indicated that the flow was uniform and axial in direction, in accordance with the design value. At -25-percent axial chord the effect of the vane leading edge was seen and the agreement between the measurements and the theory was considered very good to excellent.

(4) Comparison of the measurements and theory close to the suction surface near the leading-edge region (10- and 30-percent axial chord) indicated the possibility of some seed particle lag occurring in this region of the flow, as predicted by the particle dynamics calculation. However, the agreement in the other areas of the flow near the leading-edge region was considered very good to excellent.

(5) The largest differences between measurement and theory occurred at 80-percent axial chord. The circumferential variation in the measurements were not as smooth as in other

variation in the measurements were not as smooth as in other survey locations of the flow but the data were found to be repeatable. The origin for this behavior is not known but may have been caused by window imperfections at this axial location. The comparison with theory was still considered reasonable at this location.

(6) The measurements downstream of the vanes but close to the trailing edge plane clearly indicated the location of the vane wake. The wake deficit dissipated rapidly in moving downstream of the trailing edge and was hard to delineate at one axial chord downstream of the vanes. Outside the wake regions the measurements agreed very well with the inviscid calculations.

(7) In general, the turbulence intensity increased as the flow passed through the vane passage: it varied from about 2 to 3 percent upstream to 4 to 6 percent downstream of the vanes. Within the vane wakes, turbulence levels as high as 7 to 9 percent were measured.

References

1. Stabe, R.G.; Whitney, W.J.; and Moffitt, T.P.: Performance of a High-Work Low Aspect Ratio Turbine Tested with a Realistic Inlet Radial Temperature Profile. AIAA Paper 84-1161, June 1984 (Also, NASA TM-83655).
2. Thulin, R.D.; Howe, D.C.; and Singer, I.D.: Energy Efficient Engine High-Pressure Turbine Detailed Design Report. (PWA-5594-171, Pratt and Whitney Aircraft; NASA Contract NAS3-20646), NASA CR-165608, 1982.
3. Halila, E.E.; Lenahan, D.T.; and Thomas, T.T.: Energy Efficient Engine: High Pressure Turbine Test Hardware Detailed Design Report. (R81AEG284, General Electric; NASA Contract NAS3-20643), NASA CR-167955, 1982.
4. Yep, F.; Bush, D.; and Meyer L.: High-Work, Single-Stage, Axial-Flow Gas Generator Turbine. USAAVRADCOM-TR-83-D-4, Apr. 1983. (Avail. NTIS, AD-B073790L.)
5. Rangwalla, A.A.; Madavan, N.K.; and Johnson, P.D.: Application of an Unsteady Navier-Stokes Solver to Transonic Turbine Design. AIAA Paper 91-2468, June 1991.
6. Dominy, R.G.; and Harding, S.C.: An Investigation of Secondary Flows in Nozzle Guide Vanes. Secondary Flows in Turbomachines, AGARD CP-469, AGARD, Neuilly-Sur-Seine, France, 1990, pp. 7-1 to 7-15. (Avail. NTIS, AD-A220901.)
7. Horton, G.C.: Secondary Flow Predictions for a Transonic Nozzle Guide Vane. Secondary Flows in Turbomachines, AGARD CP-469, AGARD, Neuilly-Sur-Seine, France, 1990, pp. 8-1 to 8-12. (Avail. NTIS, AD-A220901.)
8. Wegener, D.; Quest, J.; and Hoffmann, W.: Secondary Flow in a Turbine Guide Vane with Low Aspect Ratio. Secondary Flows in Turbomachines, AGARD CP-469, AGARD, Neuilly-Sur-Seine, France, 1990, pp. 9-1 to 9-9. (Avail. NTIS, AD-A220901.)
9. Goldman, L.J.; and McLallin, K.L.: Cold-Air Annular-Cascade Investigation of Aerodynamic Performance of Core-Engine-Cooled Turbine Vanes. I. Solid-Vane Performance and Facility Description. NASA TM X-3224, 1975.
10. Goldman, L.J.; and Seasholtz, R.G.: Laser Anemometer Measurements in an Annular Cascade of Core Turbine Vanes and Comparison With Theory. NASA TP-2018, 1982.
11. Goldman, L.J.; and Seasholtz, R.G.: Three Component Laser Anemometer Measurements in an Annular Cascade of Core Turbine Vanes With Contoured End Wall. NASA TP-2846, 1988.
12. Wernet, M.P.; and Seasholtz, R.G.: Zoom Lens Compensator for a Cylindrical Window in Laser Anemometer Uses. Appl. Opt., vol. 26, no. 21, Nov. 1, 1987, pp. 4603-4611.
13. Williams, M.C.: Laser Velocimetry Study of Stator/Rotor Interactions in a Multi-Stage Gas Turbine Compressor. Advanced Instrumentation for Aero Engine Components, AGARD CP-399, AGARD, Neuilly-Sur-Seine, France, 1986, pp. 11-1 to 11-10. (Avail. NTIS, AD-A182954.)
14. Denton, J.D.: An Improved Time Marching Method for Turbomachinery Flow Calculation. J. Eng. Power, vol. 105, no. 3, July 1983, pp. 514-524.
15. Goldman, L.J.; and Seasholtz, R.G.: Comparison of Laser Anemometer Measurements and Theory in an Annular Turbine Cascade with Experimental Accuracy Determined by Parameter Estimation. Engineering Applications of Laser Velocimetry, H.W. Coleman and P.A. Pfund, eds., ASME, 1982, pp. 83-92. (Also, NASA TM-82860.)
16. Maxwell, B.R.: Particle Flow in Turbomachinery with Application to Laser-Doppler Velocimetry. AIAA J., vol. 12, no. 10, Oct. 1974, pp. 1297-1298.
17. Stevenson, W.H.; dos Santos, R.; and Mettler, S.C.: Fringe Mode Fluorescence Velocimetry. Applications of Non-Intrusive Instrumentation in Fluid Flow Research, AGARD CP-193, AGARD, Neuilly-Sur-Seine, France, 1976, pp. 20-1 to 20-9. (Avail. NTIS, 77N11221.)

REPORT DOCUMENTATION PAGE

Form Approved
OMB No. 0704-0188

1. AGENCY USE ONLY (*Leave blank*)	2. REPORT DATE	3. REPORT TYPE AND DATES COVERED
	July 1992	Technical Paper

4. TITLE AND SUBTITLE

Laser Anemometer Measurements and Computations in an Annular Cascade of High Turning Core Turbine Vanes

5. FUNDING NUMBERS

WU-505-62-52

6. AUTHOR(S)

Louis J. Goldman and Richard G. Seasholtz

7. PERFORMING ORGANIZATION NAME(S) AND ADDRESS(ES)

National Aeronautics and Space Administration
Lewis Research Center
Cleveland, Ohio 44135-3191

8. PERFORMING ORGANIZATION REPORT NUMBER

E-6354

9. SPONSORING/MONITORING AGENCY NAMES(S) AND ADDRESS(ES)

National Aeronautics and Space Administration
Washington, D.C. 20546-0001

10. SPONSORING/MONITORING AGENCY REPORT NUMBER

NASA TP-3252

11. SUPPLEMENTARY NOTES

Responsible person, Louis J. Goldman, (216) 433-5845.

12a. DISTRIBUTION/AVAILABILITY STATEMENT

Unclassified - Unlimited
Subject Category 02

12b. DISTRIBUTION CODE

13. ABSTRACT (*Maximum 200 words*)

An advanced laser anemometer (LA) was used to measure the axial and tangential velocity components in an annular cascade of turbine stator vanes designed for a high bypass ratio engine. These vanes were based on a redesign of the first-stage stator, of a two-stage turbine, that produced 75° of flow turning. Tests were conducted on a 0.771 scale model of the engine size stator. The advanced LA fringe system was designed to employ thinner than usual laser beams resulting in a 50-μm-diameter probe volume. Window correction optics were used to ensure that the laser beams did not uncross in passing through the curved optical access port. Experimental LA measurements of velocity and turbulence were obtained both upstream, within, and downstream of the stator vane row at the design exit critical velocity ratio of 0.896 at the hub. Static pressures were also measured on the vane surface. The measurements are compared, where possible, with calculations from a three-dimensional inviscid flow analysis. The data are presented in both graphic and tabulated form so that they may be readily used to compare against other turbomachinery computations.

14. SUBJECT TERMS

Turbomachinery; Turbine vanes; Annular flow; Stator vanes; Cascade flow; Optical correction procedure; Laser anemometry; Particle trajectories; Laser doppler velocimetry

15. NUMBER OF PAGES

36

16. PRICE CODE

A03

17. SECURITY CLASSIFICATION OF REPORT	18. SECURITY CLASSIFICATION OF THIS PAGE	19. SECURITY CLASSIFICATION OF ABSTRACT	20. LIMITATION OF ABSTRACT
Unclassified	Unclassified	Unclassified	

NSN 7540-01-280-5500

Standard Form 298 (Rev. 2-89)
Prescribed by ANSI Std. Z39-18
298-102

NASA-Langley, 1992